Materials Science & Engineering A 849 (2022) 143471

Contents lists available at ScienceDirect

Materials Science & Engineering A

journal homepage: www.elsevier.com/locate/msea

Coupling crystal plasticity and cellular automaton models to study meta-dynamic recrystallization during hot rolling at high strain rates

V. Shah [a,*], K. Sedighiani [a,b,e], J.S. Van Dokkum [b], C. Bos [b,e], F. Roters [a], M. Diehl [c,d]

[a] Max–Planck-Institut für Eisenforschung, Max–Planck-Str. 1, 40237 Düsseldorf, Germany
[b] Department of Materials Science and Engineering, Delft University of Technology, Mekelweg 2, 2628 CD Delft, The Netherlands
[c] Department of Materials Engineering, KU Leuven, Kasteelpark Arenberg 44, 3001 Leuven, Belgium
[d] Department of Computer Science, KU Leuven, Celestijnenlaan 200 A, 3001 Leuven, Belgium
[e] Tata Steel, Research & Development, P.O. Box 10000, 1970 CA, IJmuiden, The Netherlands

ARTICLE INFO

Keywords:
Steel
Multi-physics
Large deformation
Regridding/remeshing
Full-field simulation
Microstructure evolution

ABSTRACT

Predicting microstructure and (micro-)texture evolution during thermo-mechanical processing requires the combined simulation of plastic deformation and recrystallization. Here, a simulation approach based on the coupling of a full-field dislocation density based crystal plasticity model and a cellular automaton model is presented. A regridding/remeshing procedure is used to transfer data between the deformed mesh of the large-strain crystal plasticity model and the regular grid of the cellular automaton. Moreover, a physics based nucleation criterion has been developed based on dislocation density difference and changes in orientation due to deformation. The developed framework is used to study meta-dynamic recrystallization during double-hit compression tests and multi-stand rolling in high-resolution representative volume elements. These simulations reveal a good agreement with experimental results in terms of texture evolution, mechanical behaviour and growth kinetics, while enabling insights regarding the effect of nucleation on kinetics and crystallographic texture evolution.

1. Introduction

Hot-rolling, especially in the form of multi-stand hot-rolling, is a preferred process in industry for large and fast thickness reductions in the range of 50–99 % reduction at strain rates in the range of 10–100 s^{-1}. Elevated temperatures during hot rolling lead to recrystallization, i.e. formation of an almost dislocation free volume surrounded by High Angle Grain Boundaries (HAGBs) [1]. In industry, the concurrent occurrence of plastic deformation and recrystallization is exploited by designing and utilizing highly optimized thermo-mechanical rolling schedules [2]. Development of a thermo-mechanical rolling schedule for new steel grades requires numerous experiments and sample plant runs and is therefore an expensive endeavour.

During thermo-mechanical processing, recrystallization occurs statically, dynamically, or metadynamically. Static Recrystallization (SRX) occurs if a material after sufficient deformation is subjected to elevated temperatures resulting in the appearance and growth of deformation free crystals [1]. Recrystallization during hot deformation is termed Dynamic Recrystallization (DRX). The DRX nuclei (ideal, undistorted crystals) resulting from high mobility of HAGBs and high recovery rates at elevated temperatures, continue to grow during deformation through migration of the surrounding HAGBs [3–5]. Interruption of hot deformation or high deformation rate give insufficient time to HAGBs surrounding the DRX nuclei to migrate and consume the deformed material. In this case, these nuclei continue to grow afterwards if the temperature remains sufficiently high. Such a recrystallization process is termed Meta-Dynamic Recrystallization (MDRX) [1].

At the high strip velocities seen during industrial hot rolling, the very short times required to reach the desired reduction level result in no significant grain boundary migration during rolling [6]. Thus, grain boundary migration of the recrystallized nuclei occurs in-between the rolling passes (“*interpass annealing*”) and MDRX is observed. As MDRX affects the rolling forces and the microstructure evolution, its understanding is critical to designing sustainable hot rolling schedules for new alloys with optimized microstructures and improved properties [7].

Heavily alloyed steel grades show slow recrystallization kinetics resulting in incomplete recrystallization during interpass annealing [8]. This results in inhomogeneous microstructures that negatively influence the formability. Avoiding incomplete recrystallization while minimizing heat intake and energy consumption necessitates a good understanding of the microstructure evolution during MDRX.

---

* Corresponding author.
E-mail address: v.shah@mpie.de (V. Shah).

https://doi.org/10.1016/j.msea.2022.143471
Received 2 March 2022; Received in revised form 12 June 2022; Accepted 13 June 2022
Available online 18 June 2022
0921-5093/© 2022 The Author(s). Published by Elsevier B.V. This is an open access article under the CC BY license (http://creativecommons.org/licenses/by/4.0/).

The following approaches are available to study MDRX experimentally:

- *Stopping an industrial process*: this involves a lot of material wastage and revenue loss [9,10]. Moreover, the actual boundary conditions at a certain time or location of microstructure are not exactly known. Therefore, making inferences on material properties is difficult.
- *Laboratory scale experiments*: these have challenges of phase transformations (in steels) and machine calibration being not perfect for conditions of high temperature, high strain rates, and high deformation levels. The recrystallization process can be followed in a quasi in-situ way, where the same sample is annealed for short time intervals, probed and then annealed further [11]. Here, very short time intervals are difficult as almost instantaneous cooling after a very short annealing step is never realized [11]. This is critical in studies of MDRX after high strain rate deformation and high temperature annealing, where full recrystallization occurs in a matter of seconds [11].

The severe limitations of experimental approaches become visible when trying to capture processes during industrial rolling that involve high strain rates, high temperatures and high deformation levels [12]. In contrast, simulations allow to exactly prescribe the temperatures, strain rates and strain levels with fully observable material state. The influence of individual parameters can be assessed independently, i.e. temperature can be kept constant irrespective of strain rate or strain level. Moreover, individual parameters can be changed without affecting the other parameters, i.e. temperature can be kept constant irrespective of strain rate or strain level. This allows for the unique possibility of investigating the influence of a single parameter without the interference of other variables' effects. Strain rates far above $5\,\mathrm{s}^{-1}$, which are hard to reach in laboratory experiments, are feasible and even temperatures above $1200\,\mathrm{K}$ do not cause difficulties with data acquisition. Thus, physics-based simulations can accelerate the design process of new alloys and help in establishing optimal process conditions.

Mean field models [13], which describe the microstructure by average quantities such as flow stress, recrystallized volume fractions, and average grain sizes reach their limits when it comes to predicting nucleation which usually depends strongly on deformation heterogeneity. One reason for the strong dependency of nucleation on the local deformation state is the competition of multiple nucleation mechanisms. In low carbon steels with medium stacking fault energy, for example, discontinuous DRX [14] can nucleate either from grain boundary bulging [4,5] or development of deformation substructure into nuclei [15,16]. To describe the connection between microstructural state and nucleation, a multitude of nucleation criteria have been developed [17–19].

Full-field crystal plasticity models have emerged as powerful tools to describe polycrystalline materials' deformation [20]. Data transfer from crystal plasticity to microstructure evolution models has been proposed for modelling SRX [21–23]. However, for modelling double-hit experiments or multi-stand hot rolling, data transfer from the (partially) recrystallized microstructure is required to simulate the subsequent deformation.

Some promising approaches for full-field modelling of DRX involve coupling of microstructure models such as cellular automata [24–26], vertex methods [27], level set method [17] or phase field [18,28,29] with full-field crystal plasticity models in a continuous loop. Methods like phase field or level set methods describe grain boundary migration quite accurately [30]. However, these methods are complex to implement and associated with high computational costs. In comparison, cellular automaton approaches are easier to implement, computationally inexpensive and easy to run on parallel computers. There have also been attempts to combine crystal plasticity and microstructure evolution models into a single thermodynamically consistent framework [31,32]. However, these advanced methods are quite complex and numerically challenging. Moreover, these methods have not yet been used to model recrystallization. In all the aforementioned approaches, concurrent working of the two models and the involved data transfer between them is computationally very expensive. This leads to simulations where a compromise between simulating a large number of orientations, fine resolution and large deformation level is required. Hot deformation at high strain rates gives insufficient time for growth of the DRX nuclei [6], which results in the occurrence of grain boundary migration during annealing after the deformation step. This allows separation of these two phenomena, rendering the coupling of two models at each time step superfluous.

Crystal plasticity is often formulated in a Lagrangian setting leading to deformation of the initial spatial discretization. In contrast, cellular automata models usually work with regular grids, making direct coupling with crystal plasticity models difficult. A cellular automaton model that works on deformed grids has been outlined in [25]. However, incorporating deformed grids in cellular automata is complicated, because it leads to large computational overheads for the calculation of the transformation rules in three dimensions. One way to overcome these difficulties is to transfer the data from the deformed grid (along with fluctuations of deformation) to a regular grid for the cellular automaton using a regridding[1] approach as described by Sedighiani et al. [33]. Recently, an algorithm for implementing curvature driven grain boundary migration into a cellular automaton model has been presented [34]. However, in case of high temperature deformation, it can be assumed that the subgrains are not small enough for significant curvature driven grain boundary migration and stored energy of deformation is the only driving force considered in this work.

Here, a two-way coupling of a large-strain crystal plasticity framework (DAMASK) [35] with cellular automaton model (CASIPT) [36] is presented. The mapping between the deformed mesh of the crystal plasticity model and the regular grid of the cellular automaton is realized with the help of a recently developed regridding scheme [33]. Section 2 gives relevant details regarding DAMASK and CASIPT, and explains how these models are coupled together. The simulation setup for the different simulations performed in this paper is described in Section 3. The mechanical behaviour of recrystallized/partially recrystallized microstructures is described in Section 4.1. As recrystallized grain sizes can indicate the amount of nuclei, they are analysed and compared to experimentally observed recrystallized grain sizes in Section 4.2. Microstructure and texture evolution during a full-field multi-stand hot rolling simulation is discussed in Section 4.3. The recrystallization kinetics from the simulations are analysed in Section 4.4. Based on information from these results, we conclude that the model is able to describe MDRX correctly and well-suited for full-field simulations involving multiple deformation and annealing steps.

2. Modelling framework

The proposed modelling framework is based on two established simulation environments: DAMASK, the Düsseldorf Advanced Simulation Toolkit, for predicting the microstructure evolution during plastic deformation [35]; and CASIPT, the Cellular Automaton Sharp Interface Phase Transformation, for predicting the microstructure evolution during recrystallization [36].

---

[1] Regridding (remeshing in finite element method) refers to a process of modifying the grid (mesh) to generate a new undistorted grid to overcome the mesh distortion problem during deformation.

2.1. Crystal plasticity model — DAMASK

DAMASK is a multi-physics simulation package which uses a large-strain formulation [35]. Thanks to its flexible structure, several crystal plasticity models have been implemented into DAMASK and it has been coupled with different numerical solvers for the mechanical boundary value problem. In this work, the Fast Fourier Transform based spectral solver [37,38] and a dislocation density based constitutive law [39–41] are used. The dislocation densities evolve according to the constitutive law as follows:

$$\dot{\rho}^{\alpha}_{\mathrm{mob}} = \frac{|\dot{\gamma}^{\alpha}|}{b\Lambda^{\alpha}} - \frac{2\hat{d}}{b}\rho^{\alpha}_{\mathrm{mob}}|\dot{\gamma}^{\alpha}|; \tag{1a}$$

$$\dot{\rho}^{\alpha}_{\mathrm{dip}} = \frac{2\left(\hat{d}-\check{d}\right)}{b}\rho^{\alpha}_{\mathrm{mob}}|\dot{\gamma}^{\alpha}| - \frac{2\check{d}}{b}\rho^{\alpha}_{\mathrm{dip}}|\dot{\gamma}^{\alpha}| - \rho^{\alpha}_{\mathrm{dip}}\frac{4v_{\mathrm{climb}}}{\left(\hat{d}-\check{d}\right)}, \tag{1b}$$

where $\dot{\gamma}^{\alpha}$ is the shear rate on a particular glide system α (α is not an exponent), b is the Burgers vector magnitude, Λ^{α} is the mean free path for dislocations on slip system α, $\hat{d}$ is the distance below which two dislocations can form a dipole, $\check{d}$ is the distance below which the dislocations in dipole configuration will spontaneously annihilate each other, $\rho^{\alpha}_{\mathrm{mob}}$ is the mobile dislocation density on glide system α, $\rho^{\alpha}_{\mathrm{dip}}$ is the dipole dislocation density on glide system α and v_{climb} is the climb velocity. The two terms in Eq. (1a) describe dislocation multiplication and reduction of mobile dislocations due to dipole formation, respectively. The three terms in Eq. (1b) describe dipole formation, dipole annihilation on interaction with single mobile dislocations, and dipole annihilation through dislocation climb, respectively.

To correctly predict the dipole annihilation rates at elevated temperatures, the description for dislocation climb given in [39] has been exchanged with a model proposed by Argon and Moffat [42] that is more suitable for the considered temperatures. In the modified description, the climb velocity is given by:

$$v_{\mathrm{climb}} = 2\,\omega\exp\left(-\frac{Q_{\mathrm{cl}}}{k_{\mathrm{B}}T}\right)\left(\exp\left(\frac{\sigma_{\mathrm{cl}}b^{3}}{k_{\mathrm{B}}T}\right)-1\right), \tag{2}$$

where ω is the climb frequency factor, that is defined as $b\,\omega_{\mathrm{atomic}}\,n$ with ω_{atomic} the vibration frequency of atoms, n number of nearest neighbour sites. This means that ω is of magnitude 10^{3} ($\mathrm{m\,s^{-1}}$). k_{B} is the Boltzmann constant ($\mathrm{J\,K^{-1}}$), Q_{cl} the activation energy for the climb and σ_{cl} the climb stress on the dislocations.

The total dislocation density used in the following for the calculation of recrystallization nucleation and stored energy of deformation, is calculated as

$$\rho = \sum_{\alpha=1}^{N_{\mathrm{s}}}\left(\rho^{\alpha}_{\mathrm{mob}} + \rho^{\alpha}_{\mathrm{dip}}\right). \tag{3}$$

where N_{s} is the number of slip systems.

2.1.1. Calculation of orientation changes

The large strain formulation of DAMASK enables the prediction of change in the crystal orientation due to plastic deformation. The current orientation is obtained through polar decomposition of the elastic deformation gradient $\mathbf{F}_{\mathrm{e}} = \mathbf{R}_{\mathrm{e}}\mathbf{U}_{\mathrm{e}}$, where the elastic rotation tensor is defined as $\mathbf{R}_{\mathrm{e}} = \mathbf{O}^{\mathrm{T}}$, with $\mathbf{O}$ being the current orientation. Since $\mathbf{F}_{\mathrm{e}}$ is given with respect to a global coordinate system, the orientation will also change if the whole RVE undergoes a rigid body rotation due to the applied boundary conditions. This part of the rotation has no microstructural origin. It is therefore not of interest for local phenomena such as strain localization and needs to be removed when using the grain rotation as an indicator for recrystallization nucleation. In case of recrystallization, nuclei form when a certain cell develops high misorientation towards the neighbours. However, initiation of recrystallization occurs near grain boundary regions, where misorientations towards the neighbouring grains are already high. In such a case, the amount of "*change in orientation*", without rigid body rotation, indicates whether there is a further increase in the existing misorientations towards the neighbours. Thus, the rigid body rotation is removed from $\mathbf{F}_{\mathrm{e}}$.

The polar decomposition of the local total deformation gradient, $\mathbf{F}$, contains the rigid body rotation in the rotation tensor, $\mathbf{R}$, and dimensional changes in the stretch tensor, $\mathbf{U}$. As all the rotation goes into the rotational part of the elastic deformation gradient, $\mathbf{R}_{\mathrm{e}}$, the total rigid body rotation can be removed from it:

$$\mathbf{R}_{\mathrm{e,new}} = \mathbf{R}^{\mathrm{T}}\mathbf{R}_{\mathrm{e}}. \tag{4}$$

where $\mathbf{R}_{\mathrm{e,new}}$ is the rotation tensor of the elastic deformation gradient with no rigid body rotation component. This new elastic rotation tensor, $\mathbf{R}_{\mathrm{e,new}}$, is compared with the initial elastic rotation tensor, $\mathbf{R}_{\mathrm{e,0}}$ to get the change in orientation due to a given deformation step. Representing this change in orientation in terms of axis-angle and considering solely the angular part, gives the "*change in orientation*", $\Delta\theta$.

2.2. Cellular automaton model — CASIPT

CASIPT is a three-dimensional cellular automaton program for the simulation of the relevant metallurgical processes occurring in the annealing stage of dual-phase steels: ferrite recrystallization, pearlite-to-austenite and ferrite-to-austenite transformation during heating, and austenite-to-ferrite transformation during cooling. For the purpose of this work, it was extended to describe the grain boundary migration during meta-dynamic recrystallization of austenite.

CASIPT uses a three dimensional grid of cubic cells. For a cell of dimension δ, in three dimensions there are 6 neighbour cells at a distance δ, 12 neighbour cells at a distance $\sqrt{2}\delta$ and 8 neighbour cells at a distance $\sqrt{3}\delta$ in a full Moore neighbourhood. Each cell is given a set of properties that determine the cell's response to the transformation rules. A key feature here is that the transformation rules are applied only to cells of the interfaces between deformed and recrystallized grains. The important cell properties are:

1. **Grain ID:** Each cell is associated to a unique grain ID, g, which originates either from the initial microstructure or the formation of new grains during recrystallization. Hence, the formation of high angle grain boundaries in the grain interior during deformation is not taken into account. This simplification is justified in case of MDRX/DRX as grain fragmentation during hot deformation occurs at strains much higher than the critical strain of nucleation and thus, it is neglected. Grain IDs are used to identify interface cells and nucleation sites as well.
2. **Growth length:** Defined for each interface cell. This property is updated in each time step, Δt, by explicit Euler integration using the velocity of the interface:

   $$l(t+\Delta t) = l(t) + v\Delta t, \tag{5}$$

   where l is the growth length of an interface cell, v is the velocity at the interface cell.
3. **Energy density:** The stored energy density due to deformation is calculated from the dislocation density:

   $$E = Gb^{2}\rho, \tag{6}$$

   where E is the stored energy density, G is the shear modulus.
4. **Crystallographic Orientation:** The crystal orientation in Bunge Euler angles $\{\varphi_1;\Phi;\varphi_2\}$. For computation of misorientation related properties, the cubic symmetry of the material and the sample symmetry is taken into account.

2.2.1. Nucleation criterion

The nucleation for dynamic recrystallization is initiated by either of the mechanisms: grain boundary bulging through Strain Induced Boundary Migration (SIBM) [4,5] followed by rotation of the bulged part [4,43,44] or development of deformation substructure surrounded by HAGBs through deformation [15,16]. In both of these mechanisms, a successful nucleus is formed when there is a high stored energy difference across the interface of the grain boundary and high orientation gradients/strong rotation of material volumes. These mechanisms imply that nucleation predominantly occurs near the grain boundaries. Therefore, the following nucleation criterion is evaluated solely at the interface cells:

$$\Delta\rho \geq \Delta\rho_{\mathrm{th}} \quad \text{and} \quad \Delta\theta_{\mathrm{total}} \geq \Delta\theta_{\mathrm{th}}, \tag{7}$$

where $\Delta\theta_{\mathrm{total}}$ is the change of the cell orientation with respect to the initial orientation (without rigid body rotation) for a given cell due to deformation as described in Section 2.1.1, $\Delta\rho_{\mathrm{th}}$ is the threshold value for dislocation density difference with the neighbours, $\Delta\rho$, and $\Delta\theta_{\mathrm{th}}$ the threshold value for change in orientation, $\Delta\theta_{\mathrm{total}}$.

For detecting the nucleation sites, the threshold values $\Delta\rho_{\mathrm{th}}$ and $\Delta\theta_{\mathrm{th}}$ need to be defined. The threshold for change in orientation, $\Delta\theta_{\mathrm{th}}$ is assumed as 15°. This means that the material volume corresponding to a cell rotates at least 15° allowing formation of a HAGB [1]. For the threshold value of dislocation density difference $\Delta\rho_{\mathrm{th}}$, a physics-based criterion is developed. The starting point is static equilibrium of a spherical nucleus with radius R that grows for a positive radial driving force $f \equiv -\partial E/\partial R$. The infinitesimal energy change $\mathrm{d}E$ due to an infinitesimal increase of radius $\mathrm{d}R$ is

$$\mathrm{d}E = 8\pi\Gamma R\mathrm{d}R - 4\pi G b^2 \Delta\rho_{\mathrm{th}} R^2 \mathrm{d}R, \tag{8}$$

where Γ is the grain boundary energy. A finite and positive radial driving force leads to successful nucleation. Which leads to the following expression:

$$Gb^2\Delta\rho_{\mathrm{th}} - 2\frac{\Gamma}{R} = 0. \tag{9}$$

This criterion works well when the simulation length scale is resolved up to the subgrain size. However, the length scales of the crystal plasticity models are usually chosen to be larger to reduce computation times, i.e. the cell volume consists of multiple subgrains. Therefore, while using nucleation criterion in conjunction with the grid in crystal plasticity models, the nucleation criterion should apply for the whole cell volume. This means that the majority of the subgrains present in the cell volume should have the critical size defined by Eq. (9). The current constitutive model used in this study does not have any subgrain size evolution description. Therefore, the similitude concept [45] is invoked to calculate the size of subgrains d from the dislocation density. Thus, the subgrain size is defined as:

$$d = \frac{K}{\sqrt{\rho}}, \tag{10}$$

where K is a dimensionless material constant of the order of ten. This leads to the following minimum dislocation density difference:

$$\Delta\rho_{\mathrm{th}} = \frac{4\Gamma\sqrt{\rho}}{b^2 G K_{\mathrm{s}}}. \tag{11}$$

The dislocation density difference with the neighbours $\Delta\rho$, is defined as the maximum difference of total dislocation density between a particular cell and its neighbours belonging to other grains:

$$\Delta\rho = \max(\rho_j - \rho) \quad \text{with} \quad j \in (g_j \neq g), \tag{12}$$

where j is the index of the neighbour of a particular cell and g is the grain ID of a particular cell. The condition $j \in (g_j \neq g)$ means j belongs to neighbours having a different grain ID than the cell of interest.

When a certain cell satisfies the nucleation criterion, it is considered a nucleus and given a new grain ID. The location of each nucleus is determined at time $t_{\mathrm{a}} = 0$, where t_{a} is the annealing time. Each cell that satisfies the nucleation criterion is given an *a priori* user-defined low total dislocation density $\rho \equiv \rho_{\mathrm{low}}$.

The dislocation density in DAMASK is defined per slip system and thus, the condition $\rho \equiv \rho_{\mathrm{low}}$ should get reflected on a per slip system basis. This is done by calculating the ratio of change in dislocation density,

$$f_\rho = \frac{\rho_{\mathrm{low}}}{\rho}, \tag{13}$$

where f_ρ is the ratio of change in dislocation density determined by comparing the low dislocation density of a recrystallized cell to previous total dislocation density of the cell. This allows modification of the dislocation density on per slip system basis,

$$\begin{aligned} \rho^\alpha_{\mathrm{mob,new}} &= f_\rho \rho^\alpha_{\mathrm{mob}}, \\ \rho^\alpha_{\mathrm{dip,new}} &= f_\rho \rho^\alpha_{\mathrm{dip}}. \end{aligned} \tag{14}$$

2.2.2. Growth of the nuclei

At the start of the annealing time, $t_{\mathrm{a}} = 0$ in the cellular automaton, the identified nuclei at the interface cells start growing isotropically according to the following growth law [46]:

$$v = M\Delta P, \tag{15}$$

where M is the mobility of the grain boundary ($\mathrm{m\,Pa^{-1}\,s^{-1}}$) and ΔP is the driving pressure. The mobility of the grain boundary is a function of temperature:

$$M = M_0 \exp\left(-\frac{Q_{\mathrm{b}}}{k_{\mathrm{B}}T_{\mathrm{a}}}\right), \tag{16}$$

where M_0 is the mobility pre-factor, Q_{b} is the grain boundary migration activation energy and T_{a} the annealing temperature. The pre-factor M_0 is assumed to be constant for HAGBs.

Based on the stored energy of deformation of the particular cell and the stored energy in its neighbourhood, the driving pressure for the cells detected as nuclei can be described as,

$$\Delta P = \overline{E}_{\mathrm{N}} - E \approx \overline{E}_{\mathrm{N}}, \tag{17}$$

where E is the stored energy of deformation of cell calculated using Eq. (6) and $\overline{E}_{\mathrm{N}}$ is the average stored energy of deformation in the neighbourhood of a cell. The stored energy of the nucleus can be neglected due to the much higher dislocation density in the deformed material.

The average stored energy of deformation in the neighbourhood of a cell is described as,

$$\overline{E}_{\mathrm{N}} = Gb^2\overline{\rho}_{\mathrm{N}}. \tag{18}$$

where $\overline{\rho}_{\mathrm{N}}$ is the average dislocation density in the neighbour cells that do not share the grain ID with N being the number of such neighbour cells. The neighbour cells belonging to non-recrystallized grains are considered for calculation of average dislocation density in the neighbourhood:

$$\overline{\rho}_{\mathrm{N}} = \frac{\sum_{j=0}^{N} \rho_j}{N} \quad \text{with} \quad j \in (g_j \neq g), \tag{19}$$

Based on driving force described above, the nucleus cell grows isotropically at the velocity described by Eq. (15). The growth length is calculated according to Eq. (5). When the growth length of the cell, l, attains the grid spacings δ, $\sqrt{2}\delta$ and $\sqrt{3}\delta$, the first, second, and third nearest neighbours get transformed respectively, and are denoted as grain boundary cells. When cells of different grains grow into a shared neighbouring cell simultaneously, the neighbouring cell takes the orientation of that cell which reaches its cell centre first.

2.3. Combining DAMASK and CASIPT

DAMASK and CASIPT are independent programs simulating different types of material physics, which are coupled in this work to model different aspects of material physics together. For this purpose, the information from DAMASK is transferred to CASIPT by means of regridding and the modification of microstructure in CASIPT is reflected in the subsequent DAMASK step by changes in the relevant state variables.

2.3.1. Deformed geometry and regridding

Deformation heterogeneity of a polycrystalline material leads to grid distortion. When reaching a certain strain level, the distortion becomes too large and the simulation does not converge any more. This strain level is usually of order 0.5, but heavily dependent on many factors like constitutive law, grid resolution, morphology of grains or boundary conditions (loading conditions and temperatures). Therefore, enabling simulation of large reductions as seen in hot rolling requires overcoming of the grid distortion problem. This requires removal of the distortion and reconstruction of a new undistorted grid – a process called regridding. Additionally, such a regridding procedure resulting in a regular grid is useful for coupling with cellular automata, where a regular grid usually is a necessity.

The regridding methodology used in this study is based on the approach introduced by Sedighiani et al. [33]. In this regridding technique, a new undistorted grid is created that matches the average deformed grid in the original analysis. The original grid is then replaced by a new grid with a new spatial resolution. The deformation gradient tensor is replaced by the identity tensor and the elastic deformation is fully relaxed during regridding. The state variables from the deformed stage are mapped onto the newly created grid using a nearest-neighbour mapping algorithm. If the deformation step is not yet completed, the crystal plasticity simulation is restarted using this undistorted grid. When the deformation step is completed, regridding is done to construct an undistorted grid for the cellular automaton. At the start of CA simulation, the nucleation criterion is applied. All nuclei are treated as if they would have formed at the end of the deformation step, i.e. growth of nuclei potentially formed during the (short) deformation step is neglected. Only nuclei from the current switch are treated as nuclei due to the fast accumulation of dislocations in the nuclei from earlier generations during the deformation step.

2.3.2. Modified microstructure for the next deformation step

The microstructure evolves during the cellular automaton step, leading to changes in the spatial distribution of the dislocation density and crystal orientations. As the deformation gradient tensor is replaced by the identity tensor and elastic deformation is fully relaxed during regridding, the plastic deformation gradient is simply initialized with the new crystal orientations after the microstructure evolution, $\mathbf{F}_\mathrm{p} = \mathbf{O}_\mathrm{CA}$. Here, $\mathbf{O}_\mathrm{CA}$ is the orientation after the microstructure evolution in the cellular automaton. Correspondingly, the elastic deformation gradient also gets initialized as, $\mathbf{F}_\mathrm{e} = \mathbf{O}_\mathrm{CA}^\mathrm{T}$. The dislocation density is mapped directly to the regridded geometry to be used for further deformation.

2.3.3. Modifying orientation change of recrystallized points

In case of multi-step deformations, the total change in orientation after m_d steps can be defined as,

$$\Delta\theta_\mathrm{total}^{(m_\mathrm{d})} = \sum_{s=1}^{m_\mathrm{d}} \Delta\theta^{(s)}, \tag{20}$$

where $\Delta\theta^{(s)}$ is the change in orientation due to deformation in deformation step (s). A quantity in superscript and round brackets indicates the value of the quantity at a particular number of the deformation step. As recrystallized material behaves as virgin material, there is no need to carry over the change in orientation from previous deformation steps. If a particular material point, recrystallizes after m_d steps, the previous change in orientation is removed,

$$\Delta\theta^{(m_\mathrm{d})} = 0. \tag{21}$$

3. Simulation setup

To investigate the recrystallization behaviour predicted by the developed framework and compare it to experimental data available in the literature, following cases are considered:

1. **Double-hit compression tests**: Double-hit compression tests are widely used as experimental means to study MDRX kinetics. These experiments have shown that the rate of MDRX increases with temperature T, and strain rate $\dot{\epsilon}$ [47–50]. To allow comparison of kinetics and trends seen in simulations with existing experimental data, virtual double-hit experiments, with varying parameters such as strain rate $\dot{\epsilon}$, deformation temperature T_d, annealing temperature T_a and annealing time t_a in different combinations, as shown in Table 1 are performed. Contrary to experiments, where normally only iso-thermal conditions ($T_\mathrm{d} = T_\mathrm{a}$) are considered, non-isothermal conditions $T_\mathrm{d} \neq T_\mathrm{a}$ are also considered here. Double-hit compression tests are of interest because the deformation behaviour of recrystallized/partially recrystallized microstructures can be studied from the second deformation step.
2. **Multi-stand hot rolling**: A combination of high strain rate deformation with short interpass annealing times is frequently observed during industrial hot rolling [51,52]. As full-field microstructure data during such industrial processes is of interest, a multi-stand hot rolling process is simulated. From this simulation, the texture and microstructure evolution during industrial rolling is studied. This simulation demonstrates the capability of this modelling approach, to serve as a virtual laboratory to test different parameters of the hot rolling schedules. Moreover, a large number of orientations with fine spatial resolution are simulated, which gives statistically relevant texture evolution data, that further demonstrate the model's capabilities.
3. **Uniaxial compression followed by annealing**: To gain insights into the influence of nucleation sites and the distribution of stored energy on recrystallization kinetics, uniaxial compression followed by annealing is simulated. The nucleation sites and stored energies are varied to form following special cases: (a) *homogeneous stored energy with random nucleation*, (b) *homogeneous stored energy with non-random nucleation*, (c) *inhomogeneous stored energy with random nucleation* and (d) *inhomogeneous stored energy and non-random nucleation*. The final case of *inhomogeneous stored energy and non-random nucleation* is equivalent to of annealing of the deformed microstructure, where the nuclei are detected via the nucleation criterion described in Section 2.2.1. In all the cases considered here, the number of nuclei and the average stored energy of deformation are kept nearly constant to get comparable MDRX kinetics for all the cases. The stored energy is made homogeneous by making the dislocation density the same everywhere during the CASIPT simulation. Random nucleation is modelled by replacing the inherited change in orientation from crystal plasticity simulation by a random change in orientation fulfilling the condition of minimum misorientation. As the cases of random nucleation involve sampling from a uniform distribution, three different random samplings were simulated. The other cases use the data from the crystal plasticity simulations directly and different realizations were not considered. Here, the different realizations would be different microstructures. However, it is assumed that a microstructure with 100 grains provides sufficient statistics.

Table 1

Boundary conditions for double-hit experiments with strain rates $\dot{\varepsilon}$, deformation temperature T_d, annealing times t_a and annealing temperature T_a. The deformation temperature and strain rate remain the same for both deformation steps. The strain applied in the first and second deformation step are $\varepsilon = 0.49$ and $\varepsilon = 0.1$ respectively.

	Deformation		Annealing	
Experiment	$\dot{\varepsilon}$ (s^{-1})	T_d (K)	t_a (s)	T_a (K)
1	5.0	1373	20.0	1373
2	10.0	1373	20.0	1373
3	15.0	1373	20.0	1373
4	20.0	1373	20.0	1373
5	5.0	1223	20.0	1373
6	5.0	1273	20.0	1373
7	5.0	1323	20.0	1373
8	5.0	1373	20.0	1373
9	5.0	1373	10.0	1223
10	5.0	1373	10.0	1273
11	5.0	1373	10.0	1323
12	5.0	1373	10.0	1373
13	5.0	1373	0.0	1373
14	5.0	1373	2.5	1373
15	5.0	1373	5.0	1373
16	5.0	1373	7.5	1373
17	5.0	1373	10.0	1373

3.1. Boundary conditions

3.1.1. Double-hit compression tests

Uniaxial compression is enforced by setting average deformation gradient rate for different deformation times and complementary first Piola–Kirchoff stress as:

$$\dot{\bar{\mathbf{F}}} = \begin{bmatrix} * & 0 & 0 \\ 0 & * & 0 \\ 0 & 0 & \dot{\varepsilon} \end{bmatrix} \quad \text{and} \quad \bar{\mathbf{P}} = \begin{bmatrix} 0 & * & * \\ * & 0 & * \\ * & * & * \end{bmatrix} \tag{22}$$

The tensorial components with free deformation are represented by * in the deformation gradient rate tensor and correspondingly, it leads to a stress-free state. The tensorial components where no deformation is allowed lead to stress development represented by * in the Piola–Kirchoff stress tensor.

The deformation rate in Eq. (22) is given as per Table 1. The total logarithmic principal strain applied in the first compression stage is $\epsilon^{(1)}_\mathrm{total} \sim 0.49$ with deformation temperature T_d. Subsequently, the sample is annealed for a given period of t_a at a given temperature T_a. Finally, a second compression step $\epsilon^{(2)}_\mathrm{total} \sim 0.1$ is simulated at deformation temperature T_d, resulting in $\epsilon_\mathrm{total} = \epsilon^{(1)}_\mathrm{total} + \epsilon^{(2)}_\mathrm{total} \sim 0.6$. Annealing periods $t_\mathrm{a} = 0, 2.5, 5, 7.5, 10$, and $20\,\mathrm{s}$, annealing temperatures $T_\mathrm{a} = 1223,\ 1273,\ 1323$, and $1373\,\mathrm{K}$, deformation temperatures $T_\mathrm{d} = 1223,\ 1273,\ 1323$, and $1373\,\mathrm{K}$, and strain rates $\dot{\epsilon} = 5,\ 10,\ 15$, and $20\,\mathrm{s}^{-1}$ are used in different combinations according to Table 1. At the aforementioned strain rates, the time available for the growth of the recrystallized nuclei is insufficient for dynamic recrystallization to occur [6], allowing to apply of the microstructure evolution model only after deformation. The modelling for lower strain rates ($< 5\,\mathrm{s}^{-1}$) would be different, because at those strain rates the DRX nuclei can grow significantly during the deformation. Therefore, in such cases DRX needs to be modelled by having full coupling of deformation and microstructure evolution models during the deformation and the approach described in this paper would not be applicable.

3.1.2. Industrial multi-stand rolling

Plane strain compression is enforced by setting the average deformation gradient rate for different deformation times and complementary first Piola–Kirchoff stress as defined in Eq. (23).

$$\dot{\bar{\mathbf{F}}} = \begin{bmatrix} * & 0 & 0 \\ 0 & 0 & 0 \\ 0 & 0 & \dot{\varepsilon} \end{bmatrix} \quad \text{and} \quad \bar{\mathbf{P}} = \begin{bmatrix} 0 & * & * \\ * & * & * \\ * & * & * \end{bmatrix} \tag{23}$$

Table 2

Strain rate $\dot{\varepsilon}$, total reduction R_total, deformation temperature T_d, annealing time t_a, and annealing temperature T_a per stage of industrial multi-stand hot rolling simulations. Here, a stage refers to one process of deformation at a rolling stand followed by interpass annealing.

	Deformation			Annealing	
Stage	$\dot{\varepsilon}$ (s^{-1})	R_total (%)	T_d (K)	t_a (s)	T_a (K)
1	10	30	1373	10	1373
2	20	44	1273	5	1273
3	30	60	1223	2	1223

The strain rate per stage $\dot{\epsilon}$, total reduction after each stage R_total, interpass annealing time, deformation temperature T_d, and annealing temperature T_a are summarized in Table 2.

3.1.3. Uniaxial compression followed by annealing

Uniaxial compression is enforced by setting average deformation gradient rate $\dot{\bar{\mathbf{F}}}$ for period of $0.08\,\mathrm{s}$ and complementary first Piola–Kirchoff stress $\bar{\mathbf{P}}$ as defined in Eq. (22), with $\dot{\epsilon} = 5\,\mathrm{s}^{-1}$.

This leads to total logarithmic principal strain of $\epsilon_\mathrm{total} \sim 0.49$ with deformation temperature $T_\mathrm{d} = 1373\,\mathrm{K}$ and strain rate $\dot{\epsilon} = 5\,\mathrm{s}^{-1}$. Subsequently, the sample is annealed for a period of $t_\mathrm{a} = 20\,\mathrm{s}$ at annealing temperature $T_\mathrm{a} = 1373\,\mathrm{K}$. For these boundary conditions and the parameters as described in Tables 3 and 4, there are approximately 500 nuclei in the RVE. The details of the RVE are described in the following:

3.2. Initial microstructures

The DREAM.3D software [53] is used to create the initial microstructures used in this study. Two types of synthetic microstructures are created: One for virtual compression tests (Sections 3.1.1 and 3.1.3) and one for studying industrial multi-stand hot rolling (Section 3.1.2). The microstructure for virtual double-hit compression has a smaller number of cells and grains to allow faster simulations in comparison to the microstructure for industrial multi-stand hot rolling which needs to contain a statistically representative number of orientations. Both types of synthetic microstructures are periodic.

1. *Uniaxial compression* A microstructure with an average grain size of $95\,\mu\mathrm{m}$ is considered. The number of grid points $n_x \times n_y \times n_z$ for the initial microstructure are $44 \times 44 \times 96$, with the size of each cubic voxel being $7\,\mu\mathrm{m}$ initially. This makes the RVE size $308 \times 308 \times 672\,\mu\mathrm{m}$. There are approximately four grains in RD direction, four grains in the TD direction and eight grains in the ND direction. This leads to a RVE with 123 initial grains. The initial 3D RVE in Inverse Pole Figure (IPF) colouring is shown in Fig. 1a. The size of the RVE is determined in such a way that the uniaxial compression to a strain of $\varepsilon = 0.4$ leads to a cubic RVE. This ensures that there is no geometrical inhibition to growth of the recrystallized grains during the annealing step and results in more stable recrystallization kinetics behaviour.
2. *Plane strain compression* The number of grid points $n_x \times n_y \times n_z$ for the initial microstructure are $41 \times 25 \times 144$, with the size of each cubic voxel being $7\,\mu\mathrm{m}$ initially. This makes the RVE size $287 \times 175 \times 1008\,\mu\mathrm{m}$. The average grain size of $50\,\mu\mathrm{m}$, which is typically observed in the finishing stands of steel hot rolling, is used [54] There are approximately seven grains in RD direction, four grains in TD direction and twenty-six grains in ND direction. This leads to an RVE with 769 initial grains. The initial 3D RVE in IPF colouring is shown in Fig. 1b.

3.3. Material parameters

The parameters values used for the dislocation density based constitutive law are given in Table 3. These parameters are derived by fitting the stress strain curve at $T_\mathrm{d} = 1373\,\mathrm{K}$ and a strain rate of $\dot{\epsilon} = 5\,\mathrm{s}^{-1}$ to

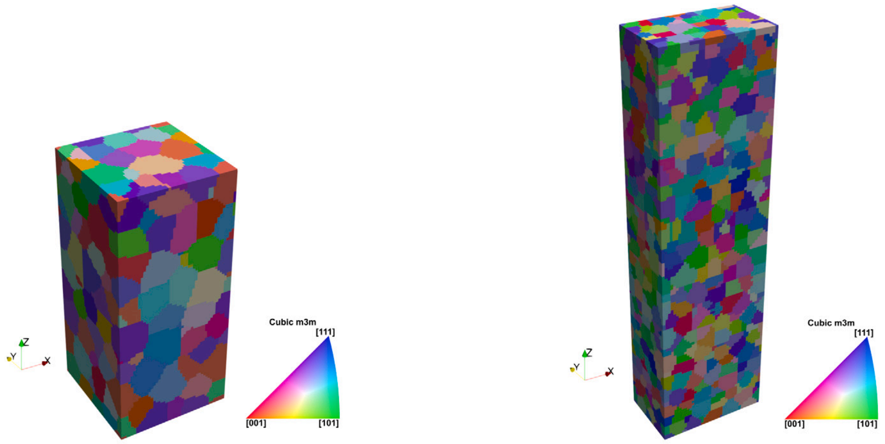

(a) (b)

Fig. 1. Inverse Pole Figure (IPF) in *z*-direction (001) of the initial microstructures used for (a) double-hit compression and (b) Industrial multi-stand hot rolling.

Table 3
Parameters used for the constitutive law in DAMASK. For the definitions of the parameters refer to earlier publications [39–41].

Parameter	Value	Unit
Lattice Structure	FCC ($N_s = 12$)	
C_{11}	50×10^9	Pa
C_{12}	32×10^9	Pa
C_{44}	47×10^9	Pa
D	2.0×10^{-5}	m
τ_0	1.5×10^8	Pa
b	2.56×10^{-10}	m
v_0	1.0×10^5	m/s
ΔF	4.5×10^{-19}	J
B	0.01	Pa s
p_{sl}	0.32	–
q_{sl}	1.46	–
$\rho_{mob,0}$	5.0×10^{13}	m^{-2}
$\rho_{dip,0}$	5.0×10^{13}	m^{-2}
Q_{cl}	4.0×10^{-19}	J
ω	900.0	m/s
D_a	8.0	–
$h^{\alpha\alpha'}$	0.122, 0.122, 0.625, 0.07, 0.137, 0.122	–

Table 4
Parameters used in the CASIPT simulation.

Parameter	Value	Unit
K_s	35	–
ρ_{low}	1.2×10^{13}	m^{-2}
M_0	1.5	Pa^{-1}s^{-1}
Q_b	2.32×10^{-19} [36]	J
Γ	0.56 [56]	Nm^{-1}

the data of Shen et al. [50] on micro-alloyed steel. It is assumed that at the temperatures studied, the precipitation of micro-alloying elements like Nb and V is not active [55] and thus, there is no influence on the stress–strain curves. The material parameters used in the CASIPT simulations are given in Table 4. The parameters regarding the intrinsic mobility M_0, and activation energy for grain boundary migration Q_b, are assumed to be for austenite [36]. The grain boundary energy, Γ, is also assumed to be those for austenite. As grain boundary energy has a wide range of available values in literature [56], a suitable value that led to a reasonable amount of nuclei was chosen as shown in Table 4.

4. Results and discussion

4.1. Mechanical response of the recrystallized/partially recrystallized microstructure

The results from the virtual double-hit compression experiments carried out as described in Section 3 and Table 1 are evaluated to ascertain whether re-introduction of the (partially) recrystallized microstructures in the crystal plasticity simulation produces the expected mechanical response. To correlate the mechanical responses with recrystallization, the evolution of recrystallized fraction X is reported. The mechanical response is evaluated based on the yield strength in the second deformation step, $\sigma_y^{(2)}$, and the hardening rate $\Theta^{(m_d)} \equiv \partial\sigma^{(m_d)}/\partial\epsilon_p$. The number in the superscript refers to the count of the deformation step.

In case of increasing strain rate or decreasing deformation temperature, the flow stress increases due to less dynamic recovery. Correspondingly, the recrystallization speeds up as seen in Figs. 2b and 3b, due to high dislocation density as a result of less dynamic recovery. Such a trend of MDRX has been reported in case of increasing strain rate [48–50]. As the annealing temperature has been kept constant during these virtual experiments, the grain boundary mobility is the same. The differences in the recrystallization kinetics is due to differences in the stored energy of deformation or due to a different number of nuclei. From the nucleation criterion described in Section 2.2.1 and Eq. (11) the required threshold value ρ_{th} increases with an increase in the dislocation density. However, individual evaluation of the threshold uses differences in the dislocation density with the neighbour cells in other grains. Increasing magnitude of dislocation density will on average lead to an increase in the value of the dislocation density difference as well. This leads to a higher number of nuclei. Each material point that satisfies the nucleation criterion is given an *a priori* user-defined low total dislocation density $\rho^i_{total} \equiv \rho_{low}$ as well. Therefore, in case of higher dislocation densities, there is a higher difference in dislocation densities between the nucleus and its neighbours, leading to a higher driving force for grain boundary migration. Thus, higher number of nuclei and higher stored energy of deformation due to higher dislocation densities lead to faster recrystallization kinetics.

Another observation from Figs. 2 and 3 is that the yield strength in the second deformation step $\sigma_y^{(2)}$ is similar to the yield strength in the first deformation step $\sigma_y^{(1)}$. This implies that after full recrystallization the material behaves like a virgin material. The flow curves from the virtual double-hit experiments for varying annealing times are shown

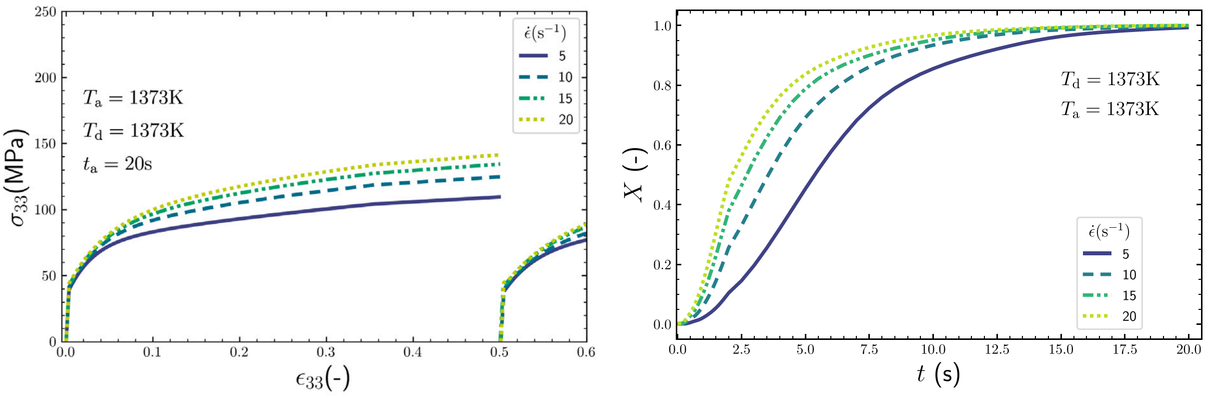

(a)

(b)

Fig. 2. (a) The flow stress σ_{33} as a function of the strain ϵ_{33} for different strain rates $\dot{\epsilon}$ =5, 10, 15, and 20 s^{-1} and (b) the recrystallized volume fraction X as a function of the annealing time t_a.

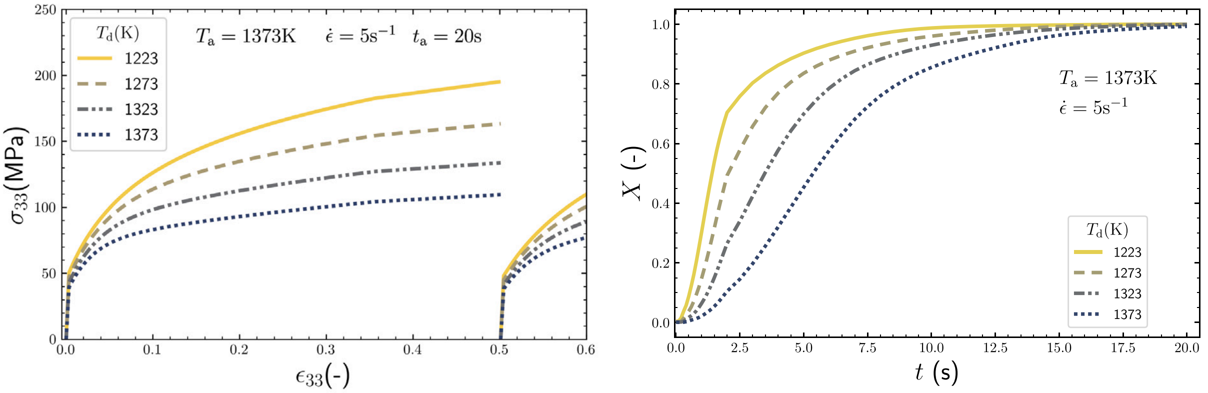

(a)

(b)

Fig. 3. (a) The flow stress σ_{33} as a function of the strain ϵ_{33} for annealing time of $t_a = 20$ s and different deformation temperatures T_d =1223, 1273, 1323, and 1373 K and (b) the recrystallized volume fraction X as a function of the annealing time t_a for the corresponding deformation temperatures T_d.

in Fig. 4a. In case of annealing time $t_a = 0$ s there is no recrystallization. Upon recrystallization, i.e. $t_a > 0$ s, the yield strength in the second deformation step, $\sigma_y^{(2)}$, decreases with annealing time. This corresponds to the evolution of recrystallized fraction, X (see Fig. 4b), where an increase in X corresponds to a decrease in $\sigma_y^{(2)}$. Increasing annealing temperature T_a also increases the recrystallization rate as seen in Fig. 5b. Here, the increasing recrystallized fraction reduces the yield strength in the second deformation step as well. As simulations have neglected static recovery, the reduction in the yield strength is attributed to MDRX alone.

Recrystallization consumes the dislocation density and forms new grains with lower dislocation density. The flow stress is proportional to the square root of the dislocation density [57]. The yield strength of the second deformation step, $\sigma_y^{(2)}$, should be close to the flow stress of the previous deformation step if there is no recrystallization. However, as recrystallization occurs, the dislocation density reduces, resulting in reduction of the yield strength of the second deformation step $\sigma_y^{(2)}$ as seen in Figs. 4a and 5a. Full recrystallization reduces the dislocation density to a minimum value and thus, the material behaves like a virgin material with similar yield strength as in the first deformation step.

From the flow stress curves in Figs. 4 and 5, one observes higher work hardening rates for the case of the partially recrystallized materials. This is confirmed by plotting the work-hardening rates $\Theta^{(1)}$ and $\Theta^{(2)}$ of the first and second compression stage, respectively, in Fig. 6. It is seen that the initial work-hardening rate in the second deformation step is higher for partially recrystallized materials with annealing times of $t_a = 2.5, 5$, and 7.5 s. This is also observed for other annealing temperatures ($T_a = 1223, 1273$ and 1323 K), where the kinetics are slower, resulting in partially recrystallized microstructures. Even though the initial work-hardening rates are high, they drop to low values very rapidly. For the case of $t_a = 10$ s and $T_a = 1373$ K in Fig. 6, 80 % recrystallization occurs and the hardening rate is always lower than during the first deformation step. In case of partially recrystallized material, there is a dislocation density contrast in the material. The recrystallized regions are quite soft and thus, harden faster in comparison to the unrecrystallized regions. This results in higher work-hardening rates, in the initial stage of the second deformation step. In the first deformation stage, the material hardens uniformly, resulting in lower work-hardening rates. The very rapid hardening in the recrystallized regions, results in attainment of faster dynamic recovery preventing further hardening. This is clearly observed in Fig. 6.

These expected mechanical responses are well captured by the model and therefore, it can be concluded that the re-introduction of recrystallized/partially recrystallized microstructure into the crystal plasticity model produces the expected mechanical response in terms of changes in the yield strength and hardening.

4.2. Recrystallized grain sizes

As number of nuclei affects the recrystallization kinetics, the average grain sizes (described in form of equivalent spherical diameter) of the fully recrystallized microstructures are studied to assess if the model predicts the correct number of nuclei. As the impingement of

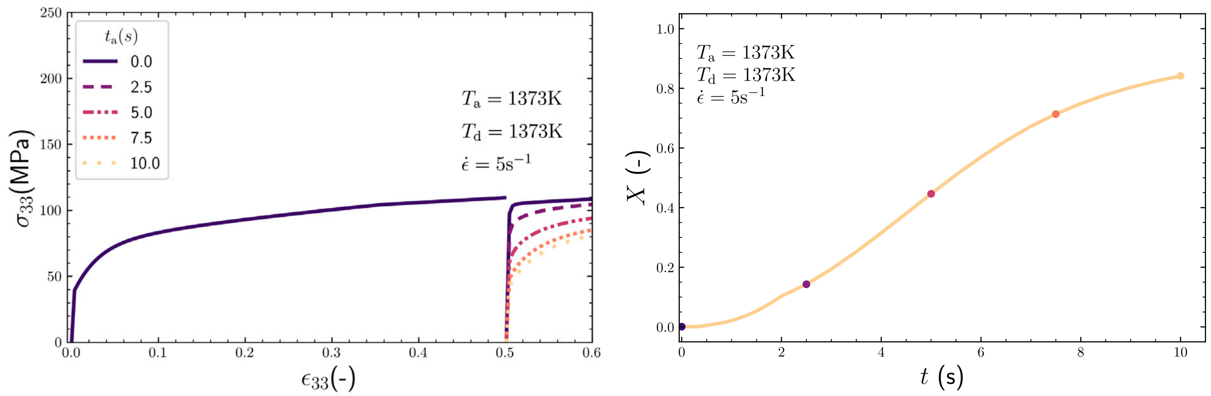

(a) (b)

Fig. 4. (a) The flow stress σ_{33} as a function of the strain ϵ_{33} for different annealing times t_a = 0, 2.5, 5, 7.5 and 10 s and (b) the recrystallized volume fraction X as a function of the annealing time t_a.

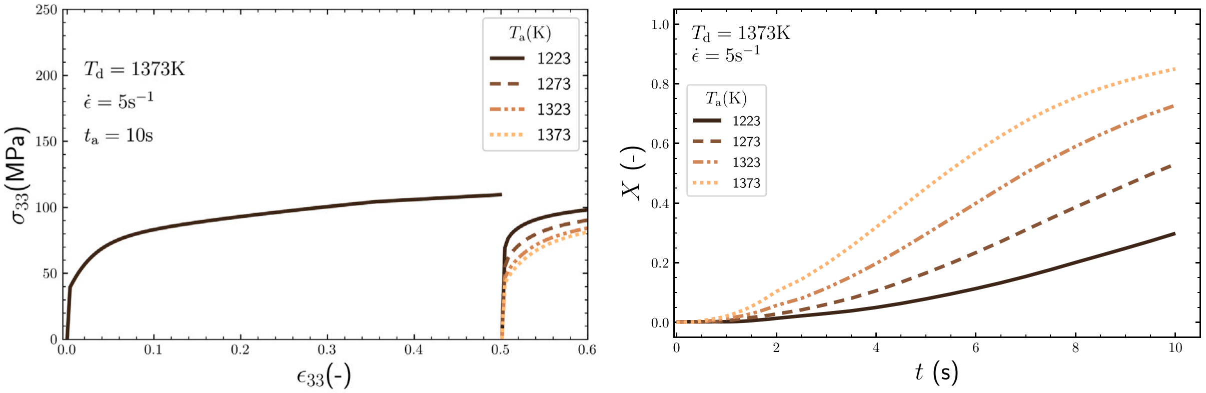

(a) (b)

Fig. 5. (a) Flow stress σ_{33} as a function of the strain ϵ_{33} for different annealing temperatures T_a =1223, 1273, 1273, and 1373 K and (b) the recrystallized volume fraction X as a function of the annealing time t_{texta} for corresponding annealing temperatures T_d.

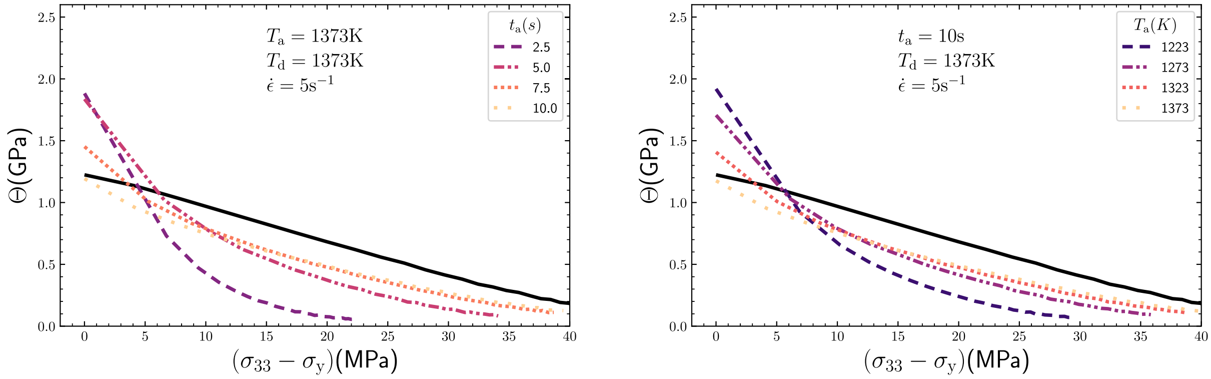

(a) (b)

Fig. 6. Work-hardening rate $\Theta^{(m_d)}$ as a function of stress above yield stress $\sigma_{33}-\sigma_y^{(m_d)}$, for first and second deformation stages, for (a) different annealing times t_a = 2.5, 5, 7.5, and 10 s and (b) annealing temperatures T_a =1223, 1273, 1323, and 1373 K. The solid black line in both the figures corresponds to the work-hardening rate for the first deformation step.

recrystallized grains leads to interruption of growth, the number of recrystallization nuclei will determine the final grain size. A large number of nuclei will lead to smaller final recrystallized grain sizes. The fully recrystallized samples from the different cases of the virtual double-hit experiments are analysed to get the average grain sizes. The fully recrystallized samples correspond to the recrystallized volume fraction curves from Fig. 2b and Fig. 3b (corresponding to case of T_d = 1273 K when annealed for t_a = 20 s). Microstructures for the cases in Fig. 2b are shown in Fig. B.12. The segmentation of the microstructure was done using DREAM.3D with a threshold misorientation for segmentation of 15°. The grain size before deformation is 95 μm. The average grain sizes for the different cases after complete recrystallization are observed to be in the range of 40–55 μm. As the strain rate increases, the grain sizes are decreasing — 53, 48, 44, and 42 μm respectively for the strain

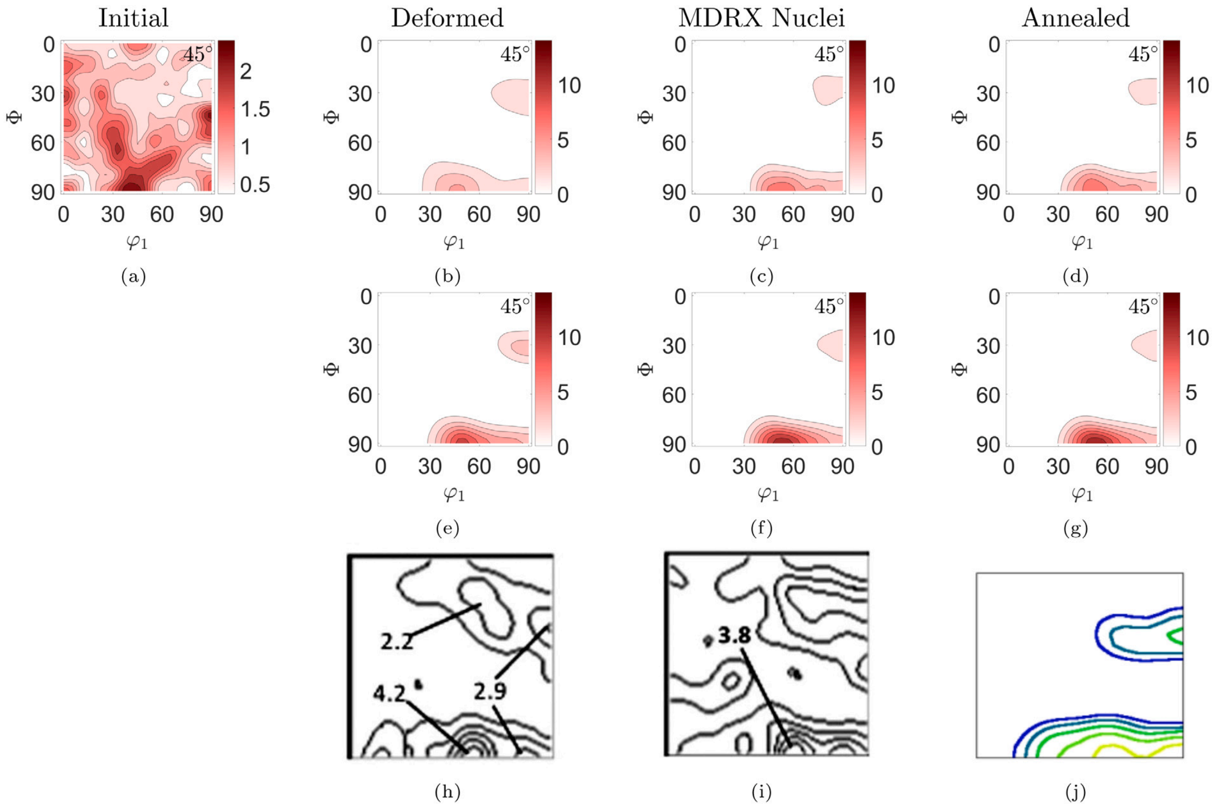

(a) (b) (c) (d) (e) (f) (g) (h) (i) (j)

Fig. 7. Texture evolution during multi-stand hot-rolling shown by ODF at different stages. The $\varphi_2 = 45°$ section is used to display the ODF. (a) Initial microstructure; (b) Strong Brass component and Copper/Dillamore components developed after thickness reduction of $R = 30\,\%$; (c) MDRX nuclei detected during first interpass annealing inherit the orientations from deformed orientations; (d) orientation inheritance leading to texture strengthening of annealed texture after first interpass annealing; (e) texture strengthening with further deformation to the thickness reduction to $R = 44\,\%$; (f) MDRX nuclei with stronger Brass component detected during second interpass annealing; (g) texture strengthening during second interpass annealing; (h) ODF of the deformed microstructure at strain of 0.2 deformed in plane strain compression at 1173 K [58]; (i) ODF of the DRX grains at strain of 0.2 deformed in plane strain compression at 1173 K [58] and (j) ODF of the fully recrystallized microstructure (Levels: 1.0, 1.40, 1.85, 2.5, 3.4, 4.7, 6.35) [59].

rates 5, 10, 15, and 20 s^{-1} at deformation temperature $T_\mathrm{d} = 1373\,\mathrm{K}$ and annealing temperature of $T_\mathrm{a} = 1373\,\mathrm{K}$. In the case of deformation temperature $T_\mathrm{d} = 1273\,\mathrm{K}$ at strain rate of $5\,\mathrm{s}^{-1}$ and annealing temperature $T_\mathrm{a} = 1373\,\mathrm{K}$ the recrystallized grain size is 43 μm. Therefore, lower deformation temperature leads to smaller recrystallized grain sizes. For comparison of grain sizes, the experimental data from the work of Shen et al. [50] is considered, where grain sizes of 43, 29, and 25 μm for the case of deformation temperature, $T_\mathrm{d} = 1273\,\mathrm{K}$, annealing temperature, $T_\mathrm{a} = 1273\,\mathrm{K}$ deformed at strain rates of 0.1, 1.0, and 5.0 s^{-1} are reported. The grain sizes found in our simulations are in a similar range and show the same trend of decreasing grain size with increasing strain rate. This allows to draw the conclusion that the number of recrystallization nuclei is correctly predicted.

4.3. Texture and microstructure evolution

In this section, the texture and microstructure evolution during the multi-stand hot rolling with interpass annealing is discussed. As there is no readily available data for texture evolution during MDRX, the texture evolution data during DRX as reported by Taylor et al. [58] is used for comparison. The texture of the initial microstructure is nearly random as seen in Fig. 7a. The ODF of the deformed microstructure after the first rolling stand is shown in Fig. 7b. The ODF given by Taylor et al. [58] (see Fig. 7h) is at strain $\varepsilon = 0.2$ at a temperature of $T_\mathrm{d} = 1173\,\mathrm{K}$, which is just after the critical strain for DRX according to their stress strain curves. At this point, the DRX nuclei have not grown significantly and therefore, the microstructure is very similar to the deformed microstructure. Thus, this ODF data right after the critical strain for DRX is used as the reference data for deformation texture. The ODF from the simulation is very similar to what has been seen typically for hot-deformed FCC metals [60,61] and in the reference data, i.e. with a strong Brass component at $\varphi_1 = 45°, \Phi = 90°, \varphi_2 = 45°$ and Copper/Dillamore component at $\varphi_1 = 90°, \Phi = 35°, \varphi_2 = 45°$ or $\varphi_1 = 90°, \Phi = 27°, \varphi_2 = 45°$. As per the assumption in the model, the MDRX nuclei are actually the DRX nuclei that do not grow during high strain rate deformation. Taylor et al. show the ODF of the DRX grains at strain $\varepsilon = 0.2$ at temperature of $T_\mathrm{d} = 900\,°\mathrm{C}$. However, the low temperature of 1173 K inhibits the grain growth and the strain is very close to the critical strain of DRX. This means that the DRX nuclei detected by Taylor et al. [58] would not have grown significantly. Thus, the MDRX nuclei from the presented simulations and the DRX nuclei from Taylor et al. are at a similar stage of microstructure development and thus amenable to comparison. The ODF of the MDRX nuclei and the DRX nuclei have similar features showing Brass and Copper/Dillamore components. This observation shows that the nucleation criterion is able to predict correct orientations of the nuclei. Considering that the nucleation criterion is active in the grain boundary regions and that texture development is dependent on the spatial distribution of orientations, getting nuclei orientations correct means that the nuclei positions are correct in a statistical sense as well. Obviously, proving that the proposed nucleation criterion detects the correct nucleation sites needs extremely difficult experiments covering different time and length scales. This requires a detailed experimental study and one-to-one comparison to simulation results and this is out of scope of this paper.

Fig. 7 shows the texture development during multi-stand hot-rolling. The ODF of the annealed microstructure (with recrystallized volume fraction of ∼ 100 %) is showing similar features as the ODF of the nuclei orientations. As the differences between the two ODFs are not significant, it can be said that the orientations of the nuclei control the texture

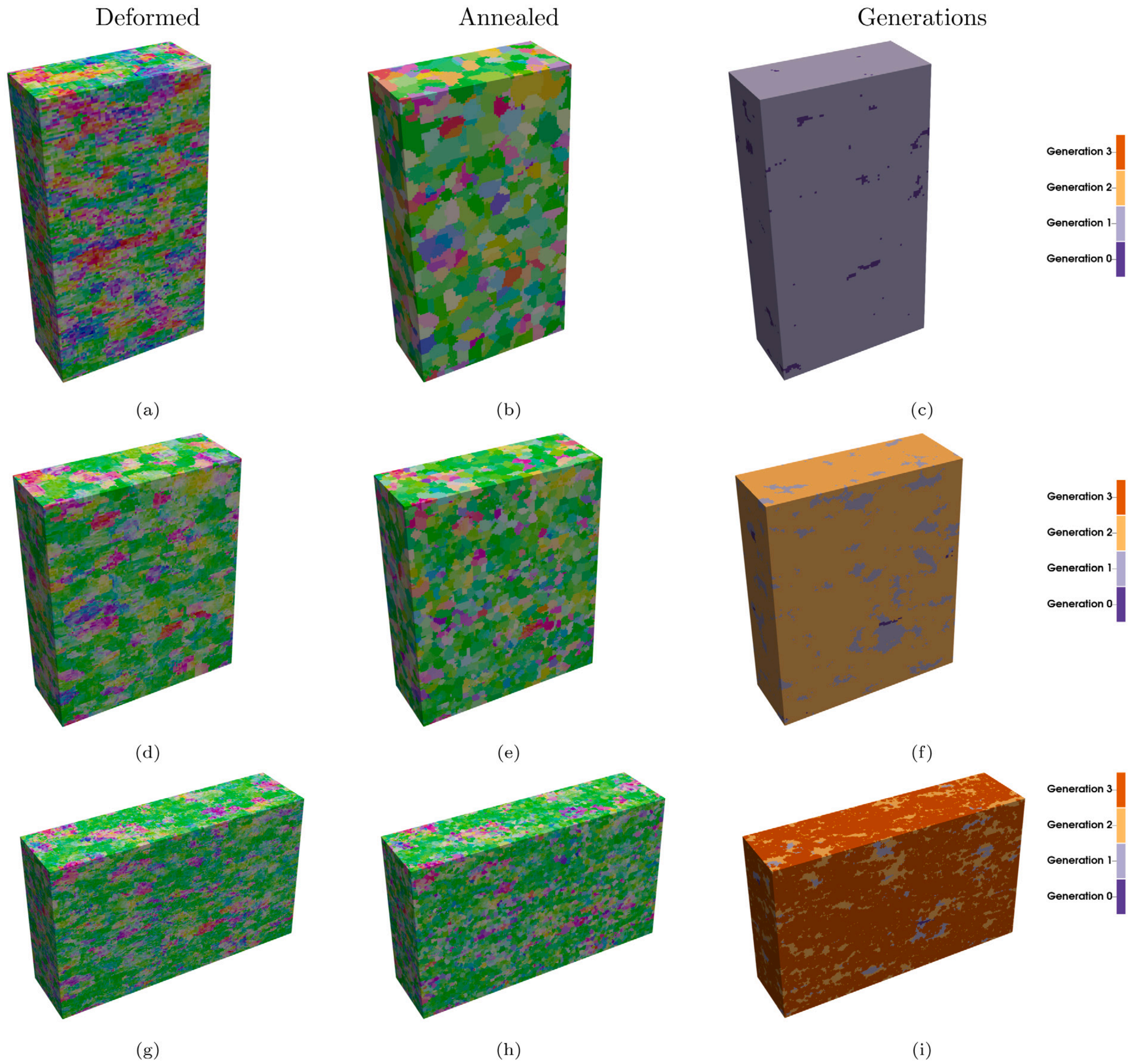

Fig. 8. Microstructure evolution during multi-stand hot-rolling shown through IPF in the z-direction (001). (a) Microstructure at thickness reduction to $R = 30\,\%$; (b) Microstructure after the first interpass annealing; (c) A map showing the generation of recrystallization volumes across the microstructure; (d) Microstructure at thickness reduction to $R = 44\,\%$; (e) Microstructure after second interpass annealing; (f) Generation map after the second interpass annealing; (g) Microstructure after thickness reduction to $R = 60\,\%$; (h) Microstructure after third interpass annealing and (i) Generation map after the third interpass annealing.

evolution during recrystallization. Assuming a similar nucleation mechanism for MDRX and SRX along with orientation inheritance of nuclei, should result in similar texture of fully recrystallized microstructure in both cases. The ODF of the annealed/recrystallized microstructure from Fig. 7d, is similar to the ODF of recrystallized austenitic high-Mn steel observed by Kestens et al. [59] (Fig. 7j). This means that the orientation evolution during growth of the nuclei is similar to the experimental observations. Moreover, orientation inheritance of the nuclei from the deformed microstructure and their dominance of the annealed texture, leads to overall strengthening of texture along the hot-rolling process (see Fig. 7). In Fig. 7, only the ODFs from the first two rolling stands are shown. In the third rolling stand, the texture intensity becomes even stronger at the same components, and therefore, not shown.

The texture strengthening is also observed in the IPF plots of the microstructure at different stages in Fig. 8. Along with the IPF plots, Fig. 8 shows the generation of the recrystallized grains as well. The generation zero corresponds to the grains that belong to the initial microstructure. Generations one, two, and three correspond to the recrystallized grains that appear during the first, second, and third interpass annealing, respectively. Fig. 8 shows that the final microstructure is a mix of recrystallized grains from different generations and even a small amount of generation zero remains. This example shows that the microstructure at different stages during the process is tracked easily and also it can be deduced as to which volume of the material corresponds to recrystallized volume from which interpass annealing stage.

4.4. Analysis of MDRX kinetics

Studying the recrystallization kinetics gives insights into the growth behaviour of the recrystallized grains in a statistical sense. Recrystallization kinetics are commonly studied by fitting the Johnson–Mehl–Avrami–Kolmogorov (JMAK) equation to the experimentally observed recrystallization volume fractions or simulation data [62,63]. The JMAK equation for the case of MDRX is commonly expressed as [64]:

$$X = 1 - \exp\left(-\mathrm{B}\left(\frac{t_{\mathrm{a}}}{t_{\mathrm{B}}}\right)^{n}\right), \tag{24}$$

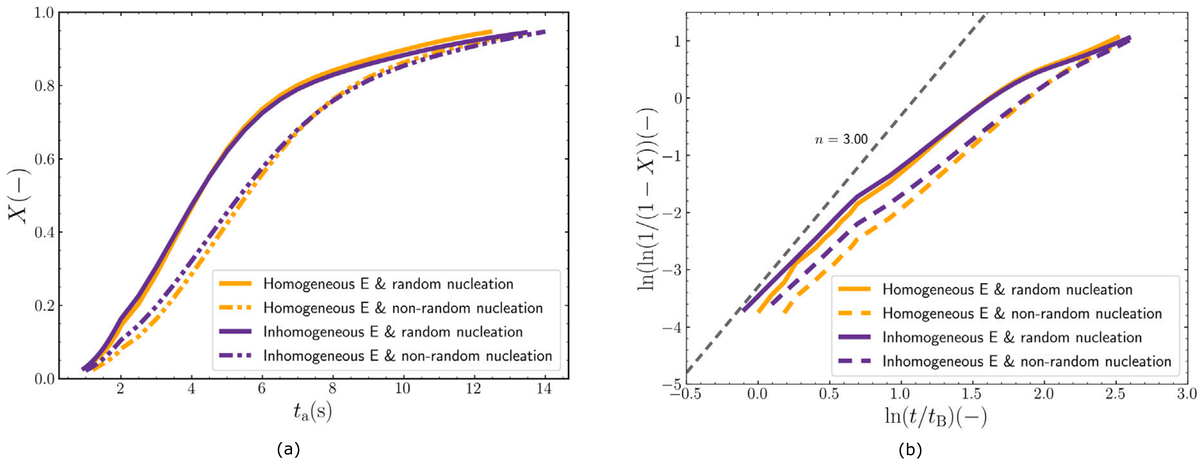

(a)

(b)

Fig. 9. (a) Recrystallized volume fraction, X, for the different cases of uniaxial compression followed by annealing: homogeneous stored energy with random nucleation (ideal case), homogeneous stored energy with non-random nucleation, inhomogeneous stored energy with random nucleation and inhomogeneous stored energy with non-random nucleation and (b) corresponding JMAK plots.

where X is the recrystallized volume fraction, t_a the inter-pass annealing time, B a dimensionless constant, t_B is the time corresponding to a given fraction of interest and n the Avrami exponent. In the section below, $t_B = 1\,\mathrm{s}$ is chosen as it aids the readability and presentation of the graphs. The recrystallized volume fraction of interest corresponding to t_B should be the same while comparing the kinetics. However, fixing $t_B = 1\,\mathrm{s}$ might lead to different recrystallized volume fractions. This is not the case here, as at $t_B = 1\,\mathrm{s}$ the recrystallized volume fractions are differing from one another within value of 0.01. Taking the natural logarithm on both sides of Eq. (24) results in,

$$\ln\left(\ln\left(\frac{1}{1-X}\right)\right) = \ln \mathrm{B} + n \ln\left(\frac{t_a}{t_B}\right), \tag{25}$$

Based on this equation, the slope of $\ln\left(t_a/t_B\right)$ against $\ln\left(\ln\left(1/1-X\right)\right)$ gives the value of the Avrami exponent n. Such plots are commonly referred to as 'JMAK-plots'. The model presented in Section 2 is validated for the recrystallization kinetics by studying the evolution of the Avrami exponent.

Applying Eq. (25) to the recrystallized volume fraction X (Fig. 9a) obtained from simulation data, leads to the JMAK plots shown in Fig. 9b. The slope of JMAK plot gives the value of the Avrami exponent n. The JMAK model predicts an Avrami exponent of three for three dimensional grain growth with site-saturated nucleation, i.e. JMAK plot is a straight line with a slope of three. However, in case of real recrystallization data, the JMAK plots deviate from this expected behaviour either through straight lines with a low Avrami exponent or they are non-linear [65,66]. The simulation data from the *uniaxial compression test followed by annealing* shows a non-linear behaviour as well, see Fig. 9b. It is similar to the plots observed in [62,67], in the sense that there is a significant decrease in slope at later stages of recrystallization. The other observation, consistent with previous observations in literature [62] for the case with *inhomogeneous stored energy and non-random nucleation*, is that the value of the Avrami exponent is lower than the value of three at all times.

As random nucleation has been modelled, different realizations for the cases which involve random nucleation have been performed. The JMAK plots for these realizations are shown in Appendix A as Fig. A.11. It is seen that the Avrami plots for the different realizations are quite close to each other. Therefore, the deviation between the different realizations is not significant and therefore, hereafter the Avrami plots for a single realization are plotted.

Among the different conditions in Fig. 9, it is obvious that the type of nucleation - *random nucleation* or *non-random nucleation* leads to a visible difference in the overall kinetics. Random nucleation cases show faster recrystallization than the cases with non-random nucleation. In contrast, the difference in kinetics arising from homogeneous and inhomogeneous stored energy of deformation is smaller. In the present simulations, the Avrami exponent does not change significantly between the cases of homogeneous and inhomogeneous stored energy of deformation. This is different from the observations of Rollet et al. [62], where different values for the Avrami exponent due to inhomogeneous stored energy of deformation have been observed. One difference is that in [62] the dislocation density varies among grains but is constant within a grain, whereas in the setup presented here the dislocation density can change from cell to cell, i.e. within grains. Moreover, the range of stored energy of deformation changes by about 50 times in simulations presented in [62] while the DAMASK simulations predict only a variation of dislocation density in the range of 20 times.

One of the reasons for deviation from the ideal JMAK behaviour is restriction of growth in certain directions due to impingement [62]. To investigate this hypothesis, the level of impingement for each recrystallized grain was tracked. This was done by going over the interface cells of a given recrystallized grain and checking if the neighbours have grain IDs belonging to other recrystallized grains. In the end, the number of different grain IDs encountered are counted to give the number of impinging grains per recrystallized grain. For the whole microstructure, the impingement values per recrystallized grain is averaged to give a single value. The mean number of impinging grains for recrystallized grains as a function of time is shown in Fig. 10.

For the case of *homogeneous stored energy with random nucleation*, the JMAK plot is shown separately in Fig. 10a. The initial (n_{initial}) and final (n_{final}) slopes of the JMAK plot are fitted. The initial regime is fitted for time $1.0 \leq t_a \leq 1.5\,\mathrm{s}$ and the final regime is fitted for $7.5 \leq t_a \leq 12.5\,\mathrm{s}$. This results in two different Avrami exponents for these two different regimes. Initially, the Avrami exponent is quite close to the expected value of three. Thereafter, the slope starts to decrease after about $1\,\mathrm{s}$. This point in time corresponds to a slight increase in the number of grains impinging each other. In case of random nucleation, the initial impingement is very low. The number of recrystallized grains impinging a given recrystallized grain keeps increasing continuously. This corresponds to a continuously decreasing Avrami exponent. At the time, when the Avrami exponent reaches the minimum value, the amount of impingement is the highest.

In case of *homogeneous stored energy with non-random nucleation* (Fig. 10b), the Avrami exponent already starts significantly lower than the theoretical value of three. This exponent value is similar to the exponent value in the previous case, when the number of impinging neighbours is between two and four (see Fig. 10a).

The significant difference in kinetics in case of random nucleation versus non-random nucleation is due to the difference in level of grain

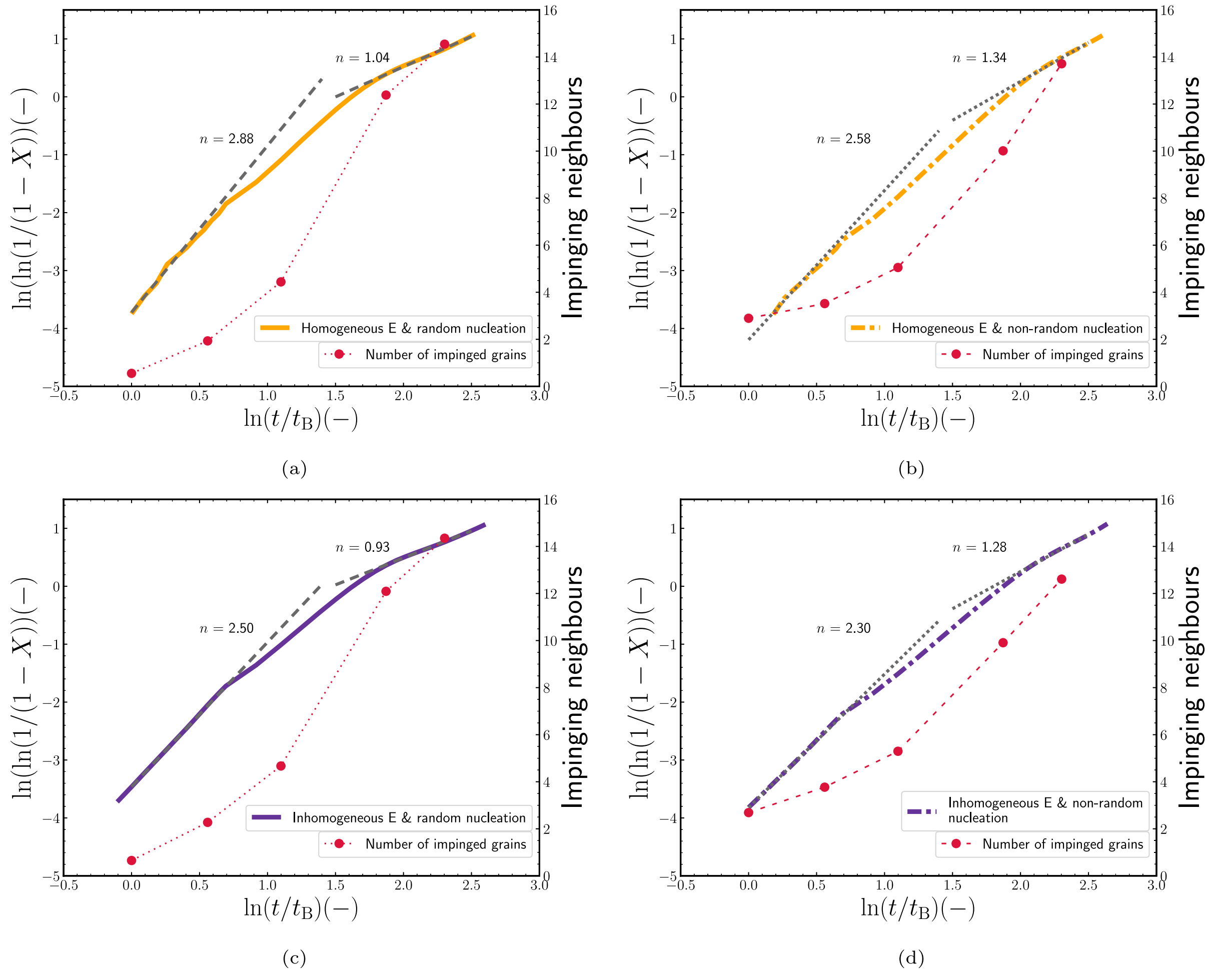

Fig. 10. JMAK plot for the different cases considered. Additionally, the number of impinging neighbours is plotted as function of annealing time (a) homogeneous stored energy and random nucleation (b) homogeneous stored energy and non-random nucleation (c) inhomogeneous stored energy and random nucleation (d) inhomogeneous stored energy and non-random nucleation.

impingement in both the cases. This can be deduced by comparison between Fig. 10a and 10b. The non-random nucleation case has higher impingement from the start resulting in lower Avrami exponent and thereby, slower recrystallization kinetics. The grain impingement prevents the growth of the recrystallized grains in the direction of the impingement. This results in growth of the recrystallized grains in less than three dimensions. Increasing impingement results in further reduction in the possible growth directions and therefore, reduction in Avrami exponent. As impingement is continuously increasing, the Avrami exponent is continuously decreasing.

The impingement situation for *inhomogeneous stored energy with random nucleation* is initially similar to the case of *homogeneous stored energy and random nucleation*. However, the initial Avrami exponent is lower. In fact, the Avrami exponent is even lower than for the case of *homogeneous energy with non-random nucleation*. The comparison of Fig. 10a and 10c shows that even inhomogeneous stored energy lowers the Avrami exponent, as inhomogeneous stored energy will not allow equal growth for all the recrystallized nuclei. However, as the overall kinetics do not show a major difference between homogeneous and inhomogeneous stored energy in Fig. 9, it can be concluded that the effect of inhomogeneous stored energy is seen only at the initial stages. The case of *inhomogeneous stored energy and non-random nucleation* has the lowest Avrami exponent at the beginning among all the cases considered. This is due to the combination of inhomogeneous stored energy and non-random nucleation at the beginning. After the initial stage, the grain impingement starts to dominate the recrystallization kinetics. Therefore, increasing grain impingement and the inhomogeneous stored energy at the beginning result in MDRX kinetics with lower than ideal Avrami exponent that continuously decreases with recrystallization. This is consistent with the results seen in the works of Rosen et al. [67] and also seen in the CA model of Hesselbarth et al. [68]. Therefore, as the model description of the growth of the recrystallized grains results in experimentally observed recrystallization kinetics, a correct description of growth in a statistical sense is confirmed.

5. Concluding remarks

A method combining a large strain crystal plasticity framework (DAMASK) with a cellular automaton model (CASIPT) along with a regridding procedure that enables simulation of multi-stand hot rolling at high strain rates is presented. Characteristic features of the mechanical response known from the experimental observations, such as, reduction in yield strength in the subsequent deformation step due to recrystallization and higher work-hardening rate of partially recrystallized microstructures due to dislocation density contrast, are reproduced by the model. The recrystallized grain size predicted by the model is in a similar range as in literature, which helps to ascertain that the number of recrystallization nuclei is predicted correctly. A good agreement is also observed for the crystallographic orientation of the nuclei which is responsible for the correct prediction of crystallographic texture. The model predicts correct nuclei orientations and positions of the nuclei. The model is able to capture the typical recrystallization kinetics seen

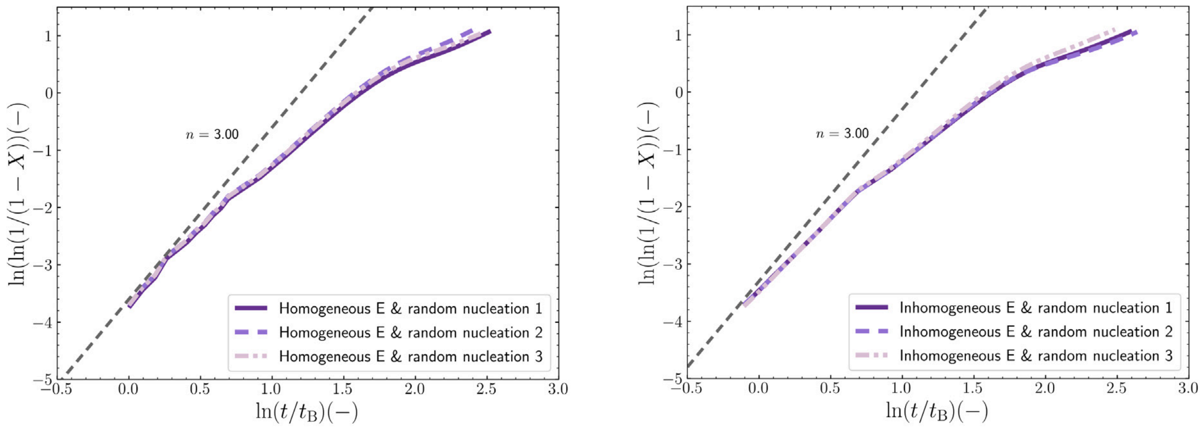

(a) (b)

Fig. A.11. (a) JMAK plot for different realizations of *homogeneous stored energy and random nucleation* and (b) JMAK plot for different realizations of *inhomogeneous stored energy and random nucleation.*

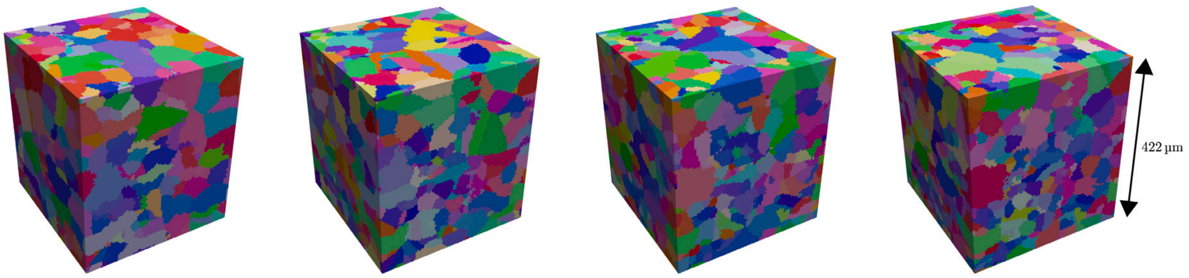

(a) (b) (c) (d)

Fig. B.12. Fully recrystallized microstructures shown as IPF in x-direction (100) for different cases mentioned in Section 4.2 deformed at $T_d = 1373\,\mathrm{K}$ and annealed at $T_a = 1373\,\mathrm{K}$ at different strain rates (a) $\dot{\epsilon} = 5\,\mathrm{s}^{-1}$, (b) $\dot{\epsilon} = 10\,\mathrm{s}^{-1}$, (c) $\dot{\epsilon} = 15\,\mathrm{s}^{-1}$ and (d) $\dot{\epsilon} = 20\,\mathrm{s}^{-1}$. The scale bar applied to all subfigures.

in the literature in the form of non-constant Avrami exponents with low values, which is mainly driven by the impingement of the recrystallized grains. This allows to conclude that the growth of the recrystallized grains is correctly described in a statistical sense. Thus, it is seen that the model is able to describe the main components of MDRX in line with the experimental observations, namely, (1) *Deformation* (2) *Number of the nuclei* (3) *Nuclei orientations* (4) *Nuclei locations* and (5) *Growth of the nuclei.*

CRediT authorship contribution statement

V. Shah: Conceptualization, Methodology, Software, Validation, Writing – original draft, Visualization. **K. Sedighiani:** Software, Methodology, Writing – review & editing. **J.S. Van Dokkum:** Validation, Writing – review & editing. **C. Bos:** Software, Writing – review & editing, Supervision, Resources. **F. Roters:** Writing – reviewing and editing, Project administration, Funding acquisition. **M. Diehl:** Software, Writing – reviewing and editing, Project administration, Funding acquisition.

Declaration of competing interest

The authors declare that they have no known competing financial interests or personal relationships that could have appeared to influence the work reported in this paper.

Data availability

The raw/processed data required to reproduce these findings cannot be shared at this time due to legal reasons.

Acknowledgements

This research was carried out under project number T17019o in the framework of the Research Program of the Materials innovation institute (M2i) (www.m2i.nl) supported by the Dutch government. V.S. would like to thank Konstantina Traka, Pablo Garcia Chao, Markus Kühbach and Dierk Raabe insightful discussions regarding recrystallization. V.S. would also like to thank Sharan Roongta, Francisco Jose Gallardo Basile and Navyanth Kusampudi for discussions related to DAMASK and data visualization. M. D. acknowledges funding by the Deutsche Forschungsgemeinschaft (DFG), Germany in the project TCMPrecipSteel (RA 659/23) in the priority program 1713 “Strong coupling of thermo-chemical and thermo-mechanical states in applied materials”.

Appendix A. Different realizations for random nucleation cases

Random nucleation is used for two cases — homogeneous stored energy and inhomogeneous stored energy. Therefore, for both of these cases, different realizations of the random nucleation are investigated. The recrystallization kinetics for these different realizations are shown in Fig. A.11.

Appendix B. Fully recrystallized microstructures

See Fig. B.12.

References

[1] F.J. Humphreys, M. Hatherly, Recrystallization and Related Annealing Phenomena, vol. 1, Elsevier, 2004, http://dx.doi.org/10.1017/CBO9781107415324.004.

[2] C.M. Sellar, G.J. Davies, Hot Working and Forming Processes, International conference organized jointly by the Sheffield Metallurgical and Engineering Association and the University of Sheffield in assocation with The Metals Society, 1979, pp. 3–15.

[3] D. Ponge, G. Gottstein, Necklace formation during dynamic recrystallization: Mechanisms and impact on flow behavior, Acta Mater. 46 (1) (1998) 69–80, http://dx.doi.org/10.1016/S1359-6454(97)00233-4.

[4] A.M. Wusatowska-Sarnek, H. Miura, T. Sakai, Nucleation and microtexture development under dynamic recrystallization of copper, Mater. Sci. Eng. A 323 (1–2) (2002) 177–186, http://dx.doi.org/10.1016/S0921-5093(01)01336-3.

[5] M. Frommert, G. Gottstein, Mechanical behavior and microstructure evolution during steady-state dynamic recrystallization in the austenitic steel 800H, Mater. Sci. Eng. A 506 (1–2) (2009) 101–110, http://dx.doi.org/10.1016/j.msea.2008.11.035.

[6] H. Zhang, K. Zhang, H. Zhou, Z. Lu, C. Zhao, X. Yang, Effect of strain rate on microstructure evolution of a nickel-based superalloy during hot deformation, Mater. Des. 80 (2015) 51–62, http://dx.doi.org/10.1016/j.matdes.2015.05.004.

[7] J. Biglou, J.G. Lenard, A study of dynamic recrystallization during hot rolling of microalloyed steels, CIRP Ann. Manuf. Technol. 45 (1) (1996) 227–230, http://dx.doi.org/10.1016/S0007-8506(07)63052-2.

[8] O. Kwon, A technology for the prediction and control of microstructural changes and mechanical properties, ISIJ Int. 32 (3) (1992) 350–358, http://dx.doi.org/10.2355/isijinternational.32.350.

[9] D. Bhattacharya, A. Mishra, G.P. Poddar, S. Misra, Case study of severe strip breakage in rolling mill of thin slab casting and rolling (TSCR) shop of TATA steel, Jamshedpur, Case Stud. Eng. Fail. Anal. 5–6 (2016) 15–22, http://dx.doi.org/10.1016/j.csefa.2015.11.002.

[10] J. Rusnák, P. Malega, J. Svetlík, V. Rudy, N. Šmajda, The research of the rolling speed influence on the mechanism of strip breaks in the steel rolling process, Materials 13 (16) (2020) http://dx.doi.org/10.3390/ma13163509.

[11] A. Nicolaÿ, G. Fiorucci, J.M. Franchet, J. Cormier, N. Bozzolo, Influence of strain rate on subsolvus dynamic and post-dynamic recrystallization kinetics of Inconel 718, Acta Mater. 174 (2019) 406–417, http://dx.doi.org/10.1016/j.actamat.2019.05.061.

[12] R.D.K. Misra, S.W. Thompson, T.A. Hylton, A.J. Boucek, Microstructures of hot-rolled high-strength steels with significant differences in edge formability, Metall. Mater. Trans. A 32 (13) (2001) 745–760, http://dx.doi.org/10.1007/s11661-001-1009-6.

[13] P. Bernard, S. Bag, K. Huang, R.E. Logé, A two-site mean field model of discontinuous dynamic recrystallization, Mater. Sci. Eng. A 528 (24) (2011) 7357–7367, http://dx.doi.org/10.1016/j.msea.2011.06.023.

[14] W. Charnock, J. Nutting, The effect of carbon and nickel upon the stacking-fault energy of iron, Met. Sci. J. 1 (1) (1967) 123–127, http://dx.doi.org/10.1179/msc.1967.1.1.123.

[15] H.E. Jiang, J. Dong, M. Zhang, Z. Yao, A study on the effect of strain rate on the dynamic recrystallization mechanism of alloy 617B, Metall. Mater. Trans. A 47 (10) (2016) 5071–5087, http://dx.doi.org/10.1007/s11661-016-3664-7.

[16] X.M. Chen, Y.C. Lin, M.S. Chen, H.B. Li, D.X. Wen, J.L. Zhang, M. He, Microstructural evolution of a nickel-based superalloy during hot deformation, Mater. Des. 77 (2015) 41–49, http://dx.doi.org/10.1016/j.matdes.2015.04.004.

[17] D.A. Ruiz Sarrazola, D. Pino Muñoz, M. Bernacki, A new numerical framework for the full field modeling of dynamic recrystallization in a CPFEM context, Comput. Mater. Sci. 179 (January) (2020) 109645, http://dx.doi.org/10.1016/j.commatsci.2020.109645.

[18] P. Zhao, T.S.E. Low, Y. Wang, S.R. Niezgoda, An integrated full-field model of concurrent plastic deformation and microstructure evolution: Application to 3D simulation of dynamic recrystallization in polycrystalline copper, Int. J. Plast. 80 (2016) 38–55, http://dx.doi.org/10.1016/j.ijplas.2015.12.010.

[19] D.G. Cram, H.S. Zurob, Y.J.M. Brechet, C.R. Hutchinson, Modelling discontinuous dynamic recrystallization using a physically based model for nucleation, Acta Mater. 57 (17) (2009) 5218–5228, http://dx.doi.org/10.1016/j.actamat.2009.07.024.

[20] F. Roters, P. Eisenlohr, L. Hantcherli, D.D. Tjahjanto, T.R. Bieler, D. Raabe, Overview of constitutive laws, kinematics, homogenization and multiscale methods in crystal plasticity finite-element modeling: Theory, experiments, applications, Acta Mater. 58 (4) (2010) 1152–1211, http://dx.doi.org/10.1016/j.actamat.2009.10.058.

[21] D. Raabe, R.C. Becker, Coupling of a crystal plasticity finite-element model with a probabilistic cellular automaton for simulating primary static recrystallization in aluminum, Modelling Simulation Mater. Sci. Eng. 8 (4) (2000) 445–462, http://dx.doi.org/10.1088/0965-0393/8/4/304.

[22] D. Raabe, Cellular automata in materials science with particular reference to recrystallization simulation, Annu. Rev. Mater. Res. 32 (1) (2002) 53–76, http://dx.doi.org/10.1146/annurev.matsci.32.090601.152855.

[23] G. Laschet, O. Güvenc, B. Böttger, T. Henke, M. Bambach, G. Hirt, M. Apel, Modelling of static recrystallization kinetics by coupling crystal plasticity FEM and multiphase field calculations, Comput. Methods Mater. Sci. 13 (2) (2013) 367–374.

[24] E. Popova, Y. Staraselski, A. Brahme, R.K. Mishra, K. Inal, Coupled crystal plasticity - Probabilistic cellular automata approach to model dynamic recrystallization in magnesium alloys, Int. J. Plast. 66 (2015) 85–102, http://dx.doi.org/10.1016/j.ijplas.2014.04.008.

[25] H. Li, X. Sun, H. Yang, A three-dimensional cellular automata-crystal plasticity finite element model for predicting the multiscale interaction among heterogeneous deformation, DRX microstructural evolution and mechanical responses in titanium alloys, Int. J. Plast. 87 (2016) 154–180, http://dx.doi.org/10.1016/j.ijplas.2016.09.008.

[26] J. Park, M. Rout, K.M. Min, S.F. Chen, M.G. Lee, A fully coupled crystal plasticity-cellular automata model for predicting thermomechanical response with dynamic recrystallization in AISI 304LN stainless steel, Mech. Mater. 167 (2022) 104248, http://dx.doi.org/10.1016/j.mechmat.2022.104248.

[27] Y. Mellbin, H. Hallberg, M. Ristinmaa, Recrystallization and texture evolution during hot rolling of copper, studied by a multiscale model combining crystal plasticity and vertex models, Modelling Simulation Mater. Sci. Eng. 24 (7) (2016) http://dx.doi.org/10.1088/0965-0393/24/7/075004.

[28] G. Abrivard, E.P. Busso, S. Forest, B. Appolaire, Phase field modelling of grain boundary motion driven by curvature and stored energy gradients. Part I: Theory and numerical implementation, Phil. Mag. 92 (28–30) (2012) 3618–3642, http://dx.doi.org/10.1080/14786435.2012.713135.

[29] G. Abrivard, E.P. Busso, S. Forest, B. Appolaire, Phase field modelling of grain boundary motion driven by curvature and stored energy gradients. Part II: Application to recrystallization, Phil. Mag. 92 (28–30) (2012) 3618–3642, http://dx.doi.org/10.1080/14786435.2012.713135.

[30] Y. Jin, N. Bozzolo, A.D. Rollett, M. Bernacki, 2D finite element modeling of misorientation dependent anisotropic grain growth in polycrystalline materials: Level set versus multi-phase-field method, Comput. Mater. Sci. 104 (2015) 108–123, http://dx.doi.org/10.1016/j.commatsci.2015.03.012.

[31] A. Ask, S. Forest, B. Appolaire, K. Ammar, O.U. Salman, A Cosserat crystal plasticity and phase field theory for grain boundary migration, J. Mech. Phys. Solids 115 (2018) 167–194, http://dx.doi.org/10.1016/j.jmps.2018.03.006.

[32] N.C. Admal, G. Po, J. Marian, A unified framework for polycrystal plasticity with grain boundary evolution, Int. J. Plast. 106 (2018) 1–30, http://dx.doi.org/10.1016/j.ijplas.2018.01.014.

[33] K. Sedighiani, V. Shah, K. Traka, M. Diehl, F. Roters, J. Sietsma, D. Raabe, Large-deformation crystal plasticity simulation of microstructure and microtexture evolution through adaptive remeshing, Int. J. Plast. 146 (2021) 103078, http://dx.doi.org/10.1016/j.ijplas.2021.103078.

[34] K. Traka, K. Sedighiani, C. Bos, J.G. Lopez, K. Angenendt, D. Raabe, J. Sietsma, Topological aspects responsible for recrystallization evolution in an IF-steel sheet – Investigation with cellular-automaton simulations, Comput. Mater. Sci. 198 (2021) 110643, http://dx.doi.org/10.1016/j.commatsci.2021.110643.

[35] F. Roters, M. Diehl, P. Shanthraj, P. Eisenlohr, C. Reuber, S.L. Wong, T. Maiti, A. Ebrahimi, T. Hochrainer, H.O. Fabritius, S. Nikolov, M. Friák, N. Fujita, N. Grilli, K.G.F. Janssens, N. Jia, P.J.J. Kok, D. Ma, F. Meier, E. Werner, M. Stricker, D. Weygand, D. Raabe, DAMASK – The Düsseldorf advanced material simulation kit for modeling multi-physics crystal plasticity, thermal, and damage phenomena from the single crystal up to the component scale, Comput. Mater. Sci. 158 (2019) 420–478, http://dx.doi.org/10.1016/j.commatsci.2018.04.030.

[36] C. Bos, M.G. Mecozzi, J. Sietsma, A microstructure model for recrystallisation and phase transformation during the dual-phase steel annealing cycle, Comput. Mater. Sci. 48 (3) (2010) 692–699, http://dx.doi.org/10.1016/j.commatsci.2010.03.010.

[37] P. Eisenlohr, M. Diehl, R.A. Lebensohn, F. Roters, A spectral method solution to crystal elasto-viscoplasticity at finite strains, Int. J. Plast. 46 (2013) 37–53, http://dx.doi.org/10.1016/j.ijplas.2012.09.012.

[38] P. Shanthraj, P. Eisenlohr, M. Diehl, F. Roters, Numerically robust spectral methods for crystal plasticity simulations of heterogeneous materials, Int. J. Plast. 66 (2015) 31–45, http://dx.doi.org/10.1016/j.ijplas.2014.02.006.

[39] S.L. Wong, M. Madivala, U. Prahl, F. Roters, D. Raabe, A crystal plasticity model for twinning- and transformation-induced plasticity, Acta Mater. 118 (2016) 140–151, http://dx.doi.org/10.1016/j.actamat.2016.07.032.

[40] K. Sedighiani, M. Diehl, K. Traka, F. Roters, J. Sietsma, D. Raabe, An efficient and robust approach to determine material parameters of crystal plasticity constitutive laws from macro-scale stress-strain curves, Int. J. Plast. 134 (2020) http://dx.doi.org/10.1016/j.ijplas.2020.102779.

[41] K. Sedighiani, K. Traka, F. Roters, D. Raabe, J. Sietsma, M. Diehl, Determination and analysis of the constitutive parameters of temperature-dependent dislocation-density-based crystal plasticity models, Mech. Mater. 164 (2022) 104117, http://dx.doi.org/10.1016/j.mechmat.2021.104117.

[42] A.S. Argon, W.C. Moffatt, Climb of extended edge dislocations, Acta Metall. 29 (1981) 293–299, http://dx.doi.org/10.1016/0001-6160(81)90156-5.

[43] D. Ponge, G. Gottstein, Necklace formation during dynamic recrystallization: Mechanisms and impact on flow behavior, Acta Mater. 46 (1) (1998) 69–80, http://dx.doi.org/10.1016/S1359-6454(97)00233-4.

[44] H. Beladi, P. Cizek, P.D. Hodgson, Dynamic recrystallization of austenite in Ni-30 Pct Fe model alloy: Microstructure and texture evolution, Metall. Mater. Trans. A 40 (5) (2009) 1175–1189, http://dx.doi.org/10.1007/s11661-009-9799-z.

[45] D.L. Holt, Dislocation cell formation in metals, J. Appl. Phys. 41 (8) (1970) 3197–3201, http://dx.doi.org/10.1063/1.1659399.

[46] D.A. Porter, K.E. Easterling, Phase Transformations in Metals and Alloys, second ed., Springer B.V., 1981.

[47] S.H. Cho, K.B. Kang, J.J. Jonas, Dynamic, static and metadynamic recrystallization of a Nb-microalloyed steel, ISIJ Int. 41 (1) (2001) 63–69, http://dx.doi.org/10.2355/isijinternational.41.63.

[48] J. Liu, Y.G. Liu, H. Lin, M.Q. Li, The metadynamic recrystallization in the two-stage isothermal compression of 300M steel, Mater. Sci. Eng. A 565 (2013) 126–131, http://dx.doi.org/10.1016/j.msea.2012.11.116.

[49] A.S. Taylor, P.D. Hodgson, The post-deformation recrystallization behaviour of 304 stainless steel following high strain rate deformation, Mater. Sci. Eng. A 529 (1) (2011) 164–169, http://dx.doi.org/10.1016/j.msea.2011.09.013.

[50] W.F. Shen, C. Zhang, L.W. Zhang, Y.N. Xia, Y.F. Xu, X.H. Shi, Metadynamic recrystallization of Nb-V microalloyed steel during hot deformation, J. Mater. Res. 32 (3) (2017) 656–665, http://dx.doi.org/10.1557/jmr.2016.486.

[51] J.J. Jonas, Dynamic recrystallization-scientific curiosity or industrial tool? Mater. Sci. Eng. A 184 (2) (1994) 155–165, http://dx.doi.org/10.1016/0921-5093(94)91028-6.

[52] H. Yada, N. Matsuzu, K. Nakajima, K. Watanabe, H. Tokita, Strength and structural changes under high strain-rate hot deformation of C steels., Trans. Iron Steel Inst. Jpn. 23 (2) (1983) 100–109, http://dx.doi.org/10.2355/isijinternational1966.23.100.

[53] M.A. Groeber, M.A. Jackson, DREAM.3D: A digital representation environment for the analysis of microstructure in 3D, Integr. Mater. Manuf. Innov. 3 (1) (2014) 56–72, http://dx.doi.org/10.1186/2193-9772-3-5.

[54] D. Liu, F. Fazeli, M. Militzer, Modeling of microstructure evolution during hot strip rolling of dual phase steels, ISIJ Int. 47 (12) (2007) 1789–1798, http://dx.doi.org/10.2355/isijinternational.47.1789.

[55] E.J. Palmiere, C.I. Garcia, A.J.D. Ardo, Compositional and microstructural changes which attend reheating and grain coarsening in steels containing niobium, Metall. Mater. Trans. A 25 (2) (1994) 277–286, http://dx.doi.org/10.1007/BF02647973.

[56] Y. Shibuta, S. Takamoto, T. Suzuki, A molecular dynamics study of the energy and structure of the symmetric tilt boundary of iron, ISIJ Int. 48 (11) (2008) 1582–1591, http://dx.doi.org/10.2355/isijinternational.48.1582.

[57] J.E. Bailey, The dislocation density, flow stress and stored energy in deformed polycrystalline copper, Phil. Mag. 8 (86) (1963) 223–236, http://dx.doi.org/10.1080/14786436308211120.

[58] A.S. Taylor, P. Cizek, P.D. Hodgson, Orientation dependence of the substructure characteristics in a Ni-30Fe austenitic model alloy deformed in hot plane strain compression, Acta Mater. 60 (4) (2012) 1548–1569, http://dx.doi.org/10.1016/j.actamat.2011.11.048.

[59] L. Bracke, K. Verbeken, L. Kestens, J. Penning, Recrystallization behaviour of an austenitic high Mn steel, Mater. Sci. Forum 558–559 (2007) 137–142, http://dx.doi.org/10.4028/www.scientific.net/msf.558-559.137.

[60] J. Hirsch, K. Lücke, Overview no. 76. Mechanism of deformation and development of rolling textures in polycrystalline F.C.C metals-II. Simulation and interpretation of experiments on the basis of Taylor-type theories, Acta Metall. 36 (11) (1988) 2883–2904, http://dx.doi.org/10.1016/0001-6160(88)90173-3.

[61] J.R. Hirsch, Correlation of deformation texture and microstructure, Mater. Sci. Technol. 6 (11) (1990) 1048–1057, http://dx.doi.org/10.1179/mst.1990.6.11.1048.

[62] A.D. Rollett, D.J. Srolovitz, R.D. Doherty, M.P. Anderson, Computer simulation of recrystallization in non-uniformly deformed metals, Acta Metall. 37 (2) (1989) 627–639, http://dx.doi.org/10.1016/0001-6160(89)90247-2.

[63] D.R. Barraclough, C.M. Sellars, Static recrystallization and restoration after hot deformation of type 304 stainless steel, Met. Sci. 13 (3–4) (1979) 257–267, http://dx.doi.org/10.1179/msc.1979.13.3-4.257.

[64] S. Choi, Y. Lee, A new approach to predicting partial recrystallization in the multi-pass hot rolling process, Met. Mater. Int. 8 (1) (2002) 15–23, http://dx.doi.org/10.1007/bf03027024.

[65] R.A. Vandermeer, P. Gordon, The influence of recovery on recrystallization in aluminum, Illinois Inst. Technol. (1962).

[66] T. Furu, K. Marthinsen, E. Nes, Modelling recrystallisation, Mater. Sci. Technol. 6 (11) (1990) 1093–1102, http://dx.doi.org/10.1179/mst.1990.6.11.1093.

[67] A. Rosen, M.S. Burton, G.V. Smith, Recrystallization of high-purity iron, Trans. AIME 230 (1964) 205–215.

[68] H.W. Hesselbarth, I.R. Göbel, Simulation of recrystallization by cellular automata, Acta Metall. Mater. 39 (9) (1991) 2135–2143, http://dx.doi.org/10.1016/0956-7151(91)90183-2.